White Rose Research Online

eprints@whiterose.ac.uk
https://eprints.whiterose.ac.uk
Universities of Leeds, Sheffield and York

Deposited via The University of Leeds.

White Rose Research Online URL for this paper:
https://eprints.whiterose.ac.uk/id/eprint/241969/

Version: Accepted Version

Article:
Gray-Wannell, N., Kershaw, C.P., Aslam, Z. et al. (2026) Probing halloysite nanotube (HNT) sorption sites using surface engineered gold or silver nanoparticles – effects of halloysite morphology and binding groups. Clays and Clay Minerals. ISSN: 0009-8604 (In Press)

https://doi.org/10.1017/cmn.2026.10039

Reuse
This article is distributed under the terms of the Creative Commons Attribution (CC BY) licence. This licence allows you to distribute, remix, tweak, and build upon the work, even commercially, as long as you credit the authors for the original work. More information and the full terms of the licence here: https://creativecommons.org/licenses/

Takedown
If you consider content in White Rose Research Online to be in breach of UK law, please notify us by emailing eprints@whiterose.ac.uk including the URL of the record and the reason for the withdrawal request.

UNIVERSITY OF LEEDS
University of Sheffield
UNIVERSITY of York

Probing halloysite nanotube (HNT) sorption sites using surface engineered gold or silver nanoparticles – effects of halloysite morphology and binding groups

Nia Gray-Wannell[1], Christopher P. Kershaw[2], Zabeada Aslam[3], James McGettrick[2], Stephen J. Hillier[1,4], Chris Greenwell[5], Rik Brydson[3], and Peter J. Holliman[2]

[1] The James Hutton Institute, Craigiebuckler, Aberdeen, AB15 8QH, UK

[2] Faculty of Science and Engineering, Swansea University, Bay Campus, Swansea, SA1 8EN, UK

[3] School of Chemical and Process Engineering, University of Leeds, Leeds, LS2 9JT, UK

[4] Department of Soil and Environment, Swedish University of Agricultural Sciences, P.O. Box 7014, SE-75007 Uppsala, Sweden

[5] Department of Earth Sciences, Durham University, Durham, DH1 3LE, UK

Corresponding author: Nia Gray-Wannell; Email: nia.gray-wannell@hutton.ac.uk

Orcid

Nia Gray-Wannell: 0000-0002-8252-5382

Zabeada Aslam: 0000-0003-3647-8965

James McGettrick: 0000-0002-7719-2958

Stephen J. Hillier: 0000-0001-9652-9950

Chris Greenwell: 0000-0001-5719-8415

Rik Brydson: 0000-0003-2003-7612

Peter J. Holliman: 0000-0002-9911-8513

Abstract

Halloysite nanotubes (HNTs) can be used as stable support materials for gold and silver nanoparticles (Au/Ag-NPs) without distinction given to the morphology of the tubular HNTs, i.e. polygonal prismatic or cylindrical. The present study aimed to use direct visualization techniques to observe and compare the adsorption sites and behaviors of the two tubular morphologies with both Au- and Ag-

NPs. Au/Ag-NPs were surface engineered with methyl-, carboxylate-, or phosphonate-terminated linker groups and reacted with halloysite nanotubes with two different morphologies, forming composite materials HNTs@Au-NPs and HNTs@Ag-NPs. Transmission electron microscopy (TEM), selected area electron diffraction (SAED), X-ray photoelectron spectroscopy (XPS), and Fourier transform infrared (FTIR) spectroscopy were used to investigate the sorption reactions. Au-NPs disperse well into individual particles while the Ag-NPs show a tendency to agglomerate, making them less suitable probes for adsorption onto HNTs. The results also indicate that polygonal prismatic HNTs show greater sorption than cylindrical HNTs, where NPs were detected on the external walls of the nanotubes. This sorption is suggested to occur at the steps and edges of the particles, at the termini of the tubes, and in the hollow inner lumina. For the varying linker groups, carboxylate- and phosphonate-derivatized Au-NPs show similar sorption behavior on HNTs, while no surface sorption was observed for the methyl-terminated linkers. This justifies the hypothesis that the carboxylate and phosphonate moieties chemisorb to the hydroxyls of the aluminol groups at the edge sites, steps, and lumina of polygonal prismatic HNTs, identifying these as key anion bonding sites on HNTs, while non-ionic, methyl-terminated Au-NPs do not adsorb. Identification of these specific anionic bonding sites on two different HNT morphologies highlights the importance of HNT morphology in their use as stable support materials in applications such as catalysis, anion sorption, and drug delivery, amongst others.

Keywords

Halloysite nanotubes; Au nanoparticles; Ag nanoparticles; TEM

(Level 1) Introduction

Halloysite is an aluminosilicate clay mineral, commonly formed in rocks and weathered soils worldwide (Joussein *et al.*, 2005) with the ideal unit formula $Al_2Si_2O_5OH_4.nH_2O$ (n = 0–2). Halloysite is a nanosized clay which ranges between 40 and 12700 nm in length with diameters of between 20 and 600 nm (Hillier *et al.*, 2016). This nanomaterial occurs naturally in a variety of morphologies, namely platy, spheroidal, and as nanotubes, with halloysite nanotubes (HNTs) being the most

common (Joussein *et al.*, 2005). Scientific and technological interest (Atyaksheva and Kasyanov, 2021; Boraei *et al*., 2024; Calvino *et al.*, 2025; Danyliuk *et al*., 2020; dos Santos *et al.*, 2017; Lin *et al*., 2017; Mazloumi *et al*., 2025; Wang *et al*., 2023; Yuan *et al*., 2015) in HNTs has increased significantly in recent years, due primarily to their attractive physical and chemical properties such as nanotubular shape, high-aspect ratio, nanoscale hollow central lumina with openings at both ends of the tubes, high length-to-diameter ratio and low toxicity *(dos Santos et al*., 2017; Vergaro *et al.*, 2010). Furthermore, the presence of aluminol surfaces in the inner layer and hollow cores of the nanotubes and external siloxane sheets results in contrasting positively charged hollow central lumina and negatively charged external surfaces (Massaro *et al*., 2017). Such unique properties allow selective modification and result in the use of HNTs and HNT nanocomposites for the controlled release of functional compounds (Lvov *et al*., 2016) with potential applications in bionanocomposites (Bertolino *et al*., 2020) and drug delivery (Melnyk *et al.*, 2025; Sharifzadeh *et al.*, 2016).

Looking specifically at the polygonal prismatic or cylindrical morphologies (Hillier *et al.*, 2016), cylindrical HNTs are characterized by their smaller particle size, in both length and diameter, with curved external surfaces, whilst their polygonal prismatic counterparts are larger in size with planar external surfaces. Recent work has shown that, in contrast to the simplistic model of halloysite nanotubes typically presented, multiple additional edge sites are present due to an abundance of steps and edges on the external siloxane surface (Gray-Wannell *et al.*, 2023). This is most noted in nanotubes with a polygonal prismatic tubular morphology. A previous study of phosphate sorption by cylindrical and polygonal HNTs (Gray-Wannell *et al*., 2020) reported that, when normalized for surface area, the smaller cylindrical HNTs show greater sorption capacity than the prismatic HNTs, though direct observation of the sorption sites on the HNTs (e.g. by spectroscopic methods) was not conclusive due to the to low sorption thresholds. The approach reported here, using phosphonate-functionalized metal nanoparticles such as Au and Ag, suggests that the phosphonate-terminated chains will adsorb to the halloysite surfaces in the same sites as phosphate anions (PO_4^{3-}) (Gray-Wannell *et al*., 2020). This approach enables visual detection of sorption sites on HNTs through observation of the attached Au/Ag nanoparticles via high-resolution TEM imaging. Furthermore, as

78 the potential effect of morphology has not been specified in other sorption studies using HNTs, the
79 present study further aimed to determine whether any effect of morphology can be observed using
80 TEM for functionalized Au/Ag-NP sorption.

81 In a wider context, this work has further application in that Au- and Ag-NPs are known to be thermally
82 stable and efficient catalysts (Massaro *et al.*, 2019). As a result, they are frequently applied in a myriad
83 of nanotechnologies as antibacterial (Burridge *et al.*, 2011; Jana *et al*., 2017), antiviral, and anti-
84 inflammatory agents (Zhang *et al.*, 2016), as well as in catalytic reactions (Mallick *et al.*, 2006), as
85 optical devices (Qu *et al.*, 2002; Rao *et al*., 2019), and in electrochemical sensing applications (Cao *et*
86 *al.*, 2012). However, attractive forces between the NPs often result in the formation of clusters, which
87 reduces their potential chemical and physical activity. This problem can be overcome by using stable
88 support materials as anchors, reducing the required loading of these expensive metals whilst
89 maintaining their potential chemical and physical efficiency. Selected support materials include zeolites
90 (Riahi *et al.*, 2002), silica (Zhang *et al.,* 2011), carbon nanotubes (Shi *et al*., 2009), and halloysite
91 nanotubes (Burridge *et al.*, 2011; Jana *et al.,* 2017; Massaro *et al.*, 2019; Sayfutdinova *et al*., 2023)
92 which were the focus of the current study in terms of the fundamental aspects of their location.

93 In the present study, three different linker molecules were combined with Au/Ag-NPs, forming
94 HNTs@Au-NPs/HNTs@Ag-NPs composite materials, to study HNT sorption sites by direct
95 visualization using TEM. All three linker molecules had a thiol group at one end of an alkyl chain to
96 bond to the Au/Ag-NPs. At the other end of the alkyl chain, two had an anionic group (carboxylate or
97 phosphonate) to probe HNTs sorption sites and the other featured a methyl group to act as a control.
98 Typically, when HNTs are considered for use as stable support materials they are functionalized by
99 linker molecules prior to addition of metal nanoparticles *(Kornilova et al*., 2021; Kumar-Krishnan *et*
100 *al.*, 2016; Massaro *et al*., 2019; Philip *et al.*, 2017). In contrast, the preset study first synthesized the
101 Au/Ag-NPs, then reacted them with the linker molecules before introducing the HNTs as stable
102 support materials. This enabled direct visualization of surface sites and ensured that any Au/Ag
103 observed on the surfaces of the HNTs is present from sorption of the anionic group which is pre-

adsorbed to the Au/Ag nanoparticles and not due to the electrostatic interaction between the Au/Ag ions and HNT surface sites.

While previous works may have studied the sorption behaviors of Au/Ag-NPs onto HNTs (Goswami *et al.*, 2019), a primary aim of the present study was to address the differences, if any, in behavior between the two tubular HNTs morphologies with both Au/Ag-NPs. The present authors suggest that the carboxyl- and phosphonate-terminated chains will adsorb directly onto the surface of the HNTs at the sites identified by previous work (Gray-Wannell *et al.*, 2020) with the objective of further highlighting previous distinctions in behavior of these two morphologies (Hillier *et al.*, 2016; Gray-Wannell *et al.*, 2020).

(Level 1) Materials and methods

(level 2) Chemicals

Dodecanethiol (methyl group, 98% purity, CAS – 112-55-0), 12-mercaptododecylphosphonic acid (phosphonic acid, 97% purity, CAS – 159239-33-5) and 11-mercaptoundecanoic acid (carboxylate, 95% purity, CAS 71310-21-9). polyvinylpyrrolidone (CAS – 9003-39-8), and dimethylformamide (CAS – 68-12-2) were obtained from Alfa Aesar. Silver nitrate (CAS – 7761-88-8) chloro(triphenlyphosphene)gold(I) (CAS – 14243-64-2) and butyl borane (CAS – 7337-45-3) were obtained from Sigma-Aldrich.

(level 2) Halloysite nanotubes (HNTs)

Both HNTs morphologies used in this study have been well characterized previously by Hillier *et al.* (2016) and Gray-Wannell *et al.* (2023) where they were identified as 4Ch and 17US. In brief, the cylindrical HNTs (4Ch) are from China and have a purity of 98.5 wt.%, as determined by X-ray powder diffraction, and a specific surface area of 80.4 m^2/g. The polygonal prismatic sample (17US) originates from the USA, has a purity of 99.0 wt.% and specific surface area of 30 m^2/g. X-ray diffraction patterns, infrared spectra, chemical compositions, and images from various microscopies for both samples can be found in the aforementioned publications.

(level 2) Synthesis of Au-NPs

Au-NPs were synthesized as described in a previous study (Li *et al.*, 2012). For the initial Au-NP experiments on both HNT morphologies, either dodecanethiol (48 µL; 0.2 mmol) or 12-mercaptododecylphosphonic acid (0.06 g, 0.2 mmol) was added. The two flasks were then stirred for 15 min, the contents transferred to sample vials and stoppered until ready for addition to the halloysites.

For the second experiment, on the polygonal prismatic HNTs with both phosphonic acid and carboxylate functional groups, the Au-NPs were synthesized in the same way. After the Au-NPs solution was divided between two flasks, 12-mercaptododecylphosphoric acid (0.0303 g; 1.07 mmol) was added to flask 1, while 11-mercaptoundecanoic acid (0.0224 g; 1.04 mmol) was added to flask 2. The two flasks were stirred for 15 min, the contents transferred to sample vials and stoppered until ready for addition to the halloysites (Fig. 1).

(level 2) Synthesis of Ag-NPs

For the Ag-NP synthesis, the capping agent, polyvinylpyrrolidone (PVP, 3.44 mol), was dissolved in 200 mL of dimethylformamide (DMF) which acted as both the solvent and reducing agent (Pastoriza-Santos and Liz-Marzán, 1999). To this solution, silver nitrate (2.5 g, 0.015 mol) was added, and the mixture was heated under reflux in an oil bath at 90°C for 6 h until the solution turned a deep yellow. The yellow color coincided with the formation of the Ag-NPs with particle size of ~5–10 nm (Van Hyning and Zukoski, 1998). An aliquot of 1 mL of solution was pipetted into an Eppendorf centrifuge tube and 0.2 mL of ethanol added. The samples were centrifuged for 30 s, the supernatant decanted off and replaced with a further 1 mL of ethanol. The suspension was hand shaken. The preceding stage required splitting of the solutions between two separate, round-bottomed flasks where the solution from 20 Eppendorf tubes was rinsed into each flask and were further diluted with 20 mL of ethanol. Linker molecules were added to each flask where flask 1 contained the phosphonic acid linker, 12-mercaptododecylphosphonic acid (0.0303 g, 1.07 mmol), while, to flask 2 the carboxylate linker, 11-mercaptoundecanoic acid (0.0227 g, 1.04 mmol) was added. Both flasks were stirred for 15 min after the addition of the linker molecules before being stoppered.

(level 2) Addition of HNTs to Au/Ag-NP solutions to form HNTs@Au-NPs/HNTs@Ag-NPs composite materials

100 mg of each halloysite was weighed out and mixed with 3 mL of nanoparticle/linker solution along with 3 mL of ethanol. Each sample was sonicated in a sonic bath at room temperature for 10 min and left to settle overnight. The following day the samples were sonicated for a further 10 min and centrifuged. All samples were dried under vacuum.

(level 2)Analytical techniques

The size of the Au-NPs was measured using a Perkin Elmer Lambda 35 UV/Vis spectrometer (Supplementary information, Fig. S1) with a scan range of 250–700 nm and after heating the UV lamps for 15 min.

Fourier Transform infrared (ATR-FTIR) analysis was conducted on all vacuum-dried samples using a Bruker Vertex 70 Fourier Transform infrared spectrometer in the mid-infrared region from 4000 to 400 cm^{-1} with a scan rate of 200 scans per spectrum. The samples were dry-air purged during analysis to reduce interference from water and carbon dioxide.

X-ray photoelectron spectroscopy (XPS) analysis (using a KRATOS AXIS SUPRA instrument with a monochromated AlKα source and a beam footprint of 700 μm on the x-axis and 300 μm on the y-axis) was used in the first set of experiments to identify the presence of phosphorus, gold, and sulfur groups on the external surfaces of the halloysites. Samples were loaded as vacuum-dried powders onto carbon strips and evacuated in situ before analysis. Survey scans at a pass energy of 160 eV were used to identify individual elements present, with a typical set of high-resolution spectra then run at a pass energy of 40 eV and step size of 0.1 eV, with a minimum dwell time of 1000 ms. Both the dwell time and the number of sweeps were increased as necessary to improve the S:N ratio for elements with small atomic concentrations. The integral charge neutralizer was used throughout and peaks were calibrated to the main hydrocarbon (contamination) peak at 284.8 eV; the data was analyzed using *CASAXPS* version 2.3.26PR1.0. Peak areas were estimated by applying Shirley backgrounds, except in the case of P(2p) where a negative gradient to the control background made use of a linear

182 background more appropriate. Where peaks were fitted, the GL(30) lineshape was used.
183 Quantification used the KratosPlus sensitivity factor library.

184 Simultaneous Thermal Analysis (STA) was conducted using a Perkin-Elmer STA 6000 instrument
185 which had been calibrated to the melting points of indium and silver. An air-flow rate of 19.8 mL/min
186 was used for a continuous run from 30 to 600°C with a 10°C/min ramp rate. The STA data were
187 recorded for samples with gold nanoparticles with either phosphonic acid- or methyl-terminated linkers.

188 A ThermoFischer Titan Themis TEM instrument was used to record bright field images of the surfaces
189 of the HNTs@Au-NPs and HNTs@Ag-NPs. The samples were dispersed in methanol and drop cast
190 onto an amorphous holey carbon film mounted on a 3 mm copper grid. The TEM was operated at
191 300 kV and was fitted with a monochromator enabling control over the electron dose. The high
192 sensitivity of HNTs to the electron beam resulted in a beam current of ~0.5 nA being employed. In situ
193 EDX spectroscopy confirmed the presence of the Au/Ag-NPs and in situ SAED patterns were recorded
194 to verify the dehydrated state of the halloysite nanotubes and the presence of gold. The EDX data were
195 collected using a Super-X EDX system with a 4-windowless design and further processed using
196 Velox©. Images and diffraction patterns were captured using a Gatan Oneview 16-megapixel CMOS
197 digital camera. The TEM CMOS camera employed comprises 4k by 4k pixels and the image pixel size
198 used for sizing the nanoparticles varied between 0.0625 and 0.0450 nm, depending on the exact image
199 magnification.

200 **(level 1) Results**

201 **(level 2) Confirmation of Au-NPs on the surface of cylindrical and polygonal prismatic HNTs**

202 The following methods: XPS, FTIR, SAED, and TEM, were used to establish the sorption of the Au-
203 NPs via their linker molecules onto the halloysite surface of the two HNT morphologies.

204 X-ray photoelectron spectroscopy (XPS) confirmed the presence of gold (1.3 at.%, 1.4 at.%), sulfur
205 (0.2 at.%, 0.3 at.%) and phosphate groups (0.9 at.% and 1.2 at.%) on the external surfaces of both the
206 cylindrical and polygonal prismatic nanotubes, respectively, when the Au-NPs with phosphonic acid-
207 terminated linkers were used (Table 1, Table S1, Figs S2–S9).

Fourier transform infrared (FTIR) spectroscopy of the two HNT morphologies with Au-NPs derivatized either with phosphonic acid- or methyl-terminated linkers showed subtle differences in their spectra (Fig. 2, Fig. S10). For the control experiment, no evidence was found of methyl-terminated linkers adsorbed to the surfaces of either cylindrical or polygonal prismatic HNTs despite this linker molecule (dodecanethiol) possessing a similar number of C–H bonds to 12-mercaptododecylphosphonic acid. This suggests that chemisorption through the phosphonate anion is the key binding mode for these linkers and that the methyl-terminated Au-NPs do not have a strong affinity for the HNTs.

Simultaneous thermal analysis (STA) simultaneously measures thermogravimetry (TGA) and differential scanning calorimetry (DSC). The TGA analysis of the polygonal prismatic HNT with Au-NPs and methyl terminated linkers (Fig. S11) showed a smaller mass loss (15.0%) while the polygonal prismatic HNT sample with Au-NPs and phosphonic acid-terminated linkers (Fig. S12) showed a 17.0% mass loss. Given that the XPS data which indicated only the phosphoric acid-terminated Au-NPs sorb onto halloysite, this suggests that 2.0% of the total sample mass can be attributed to the Au-NPs with the phosphate linker as the composite material HNTs@Au-NPs was formed.

In line with this, the TGA data indicated that the cylindrical sample HNT with Au-NPs and methyl-terminated linker showed a lower mass loss of 15.5% over the same temperature range (Fig. S13), whilst the sample cylindrical HNTs with Au-NPs and phosphonic acid terminated linker (Fig. S14) showed an 18.0% mass loss over the temperature range 30–800°C. Again, considering the XPS data, where it appeared that only the Au-NPs with phosphonic acid-terminated linkers sorb onto the external halloysite surface, suggests that 2.5% of the sample mass of the phosphonic acid-terminated linker sample can be attributed to the Au-NPs and linker.

The TEM and SAED were conducted on both the untreated nanotubes and those reacted with the Au-phosphonic-acid moiety (Fig. 3). The presence of gold was confirmed from the *d* spacings measured at 1.2 and 0.9 Å in Fig. 3b,d (Table S2).

Imaging by TEM was employed to visualize the distribution of Au/Ag-NPs as they scatter electrons strongly relative to HNTs support. From the images obtained (Figs 4, S15), the observed features on the HNTs surfaces have been confirmed as Au-NPs using in situ EDX spectroscopy (Fig. S16). Analysis of the TEM images suggested that the Au-NPs were present as spheres and the *ImageJ* software was used to measure their size as 1.88 ± 1.00 nm (n = 819). The average size of the Au-NPs was confirmed using UV-vis spectroscopy which measured the Au-NPs size as between 1 and 2 nm (Fig. S1).

Given the greater visibility of Au-NPs on the polygonal prismatic HNTs it was considered that the subsequent experiments should focus on this morphology only and expand on the NPs and linker molecules studied. Hence, TEM and FTIR analysis were conducted on a further set of polygonal prismatic HNTS which had been treated with Au-NPs and Ag-NPs with both phosphonic acid- and carboxylate-terminated linkers.

(level 2) Comparison of phosphonic- and carboxylate-terminated linker sorption on polygonal prismatic HNTs using both Au- and Ag-NPs

The presence of polyvinylpyrrolidone in the Ag-NP spectra (Huang *et al*., 2019) with a C=O band at ~1662 cm^{-1}, C–N bands between 1288 and1435 cm^{-1} and a broad N-H peak at ~3336 cm^{-1} (Fig. 5b,c) all indicated the presence of the Ag-NPs. The FTIR analysis of the samples with phosphonic acid- or carboxylate-terminated linkers on polygonal prismatic HNTs again showed evidence of chemisorption via phosphonate or carboxylate esters, respectively. For example, after Au-NPs sorption, a reduction in intensity of up to 50% was calculated for the 3670 cm^{-1} Al–OH stretching band (Fig. 5d,5e), indicating sorption at these sites. For the Ag-NPs with both carboxylate and phosphonic acid-terminated linkers the peak at 3670 cm^{-1} was indistinct and therefore impossible to measure.

An interesting observation can be made about the different behaviors of the Au- and Ag-NPs as observed by TEM (Fig. 6), where, for the HNTs@Au-NPs, the NPs appeared clearly to adsorb onto the surface of the halloysite nanotubes at distinct sites. From Fig. 6, there is little or no visible distinction in frequency and distribution of Au-NPs when the two types of linker molecule, phosphonic acid (Fig. 6a,b) and carboxylate (Fig. 6c,d), are compared. Due to the natural variation in the sizes of Au-NPs, some of the individual HNTs showed the nanoparticles on the surface more clearly than others. This

can be seen by comparing Figs 6c and 6d. The data measured using the *ImageJ* software showed two nanotubes from the same sample but the average nanoparticle sizes in Fig. 6c are 2.66 ± 1.03 nm (n = 99) compared to 1.71 ± 0.60 nm (n = 95) measured in Fig. 6d. The images in Fig. 7 again suggested that the aluminol sites at the termini of the nanotubes and those in the inner lumina and at steps and edges on the external surfaces are where the chemisorption occurs.

As for the Au-NPs, the Ag-NPs are observed to be primarily spherical in shape, and their diameter was measured as an average of 3.11 ± 1.89 nm (n = 64). In contrast to the apparent individual sorption behavior displayed in the HNTs@Au-NPs composite materials with phosphonic acid- and carboxylic acid-terminated linkers, the HNTs@Ag-NPs with both phosphonic acid- and carboxylate-terminated linkers showed agglomeration. These agglomerates resulted in clusters that contain hundreds of Ag-NPs (Fig. S17).

(level 1) Discussion

In the XPS analysis, phosphorous was shown by XPS to be in two distinct chemical states in the Au-NP-treated samples: one peak was consistent with metal-phosphate, and the other with a less oxidized phosphorus which resembled a metal-coordinated PR_3 organic species (Fig. S7). This could also be explained by some phosphate which has reacted, lost oxygen and formed a new chemical bond. The S 2p position matched that of an Au-S-R chemical bond. For the control experiments using methyl-terminated linker, the data showed zero or trace gold levels (0.0, 0.1 at.%) for the cylindrical and polygonal prismatic HNTs, respectively. Given that XPS sensitivity is ~0.1 at.% the gold levels on the methyl-terminated linker for the polygonal prismatic HNTs were seen as being at, or below, the limit of detection. Hence, as expected, it can be assumed that surface sorption was not occurring at a detectable level with the methyl-terminated linkers. These control experiments supported the hypothesis that only the anionic phosphate linkers can chemisorb to the halloysite surface (Fig. 1).

The subtle differences in FTIR spectra of the two HNT morphologies with Au-NPs derivatized either with phosphonic acid- or methyl-terminated linkers (Fig. 2, Fig. S10) can be explained partially because the HNTs dominated the spectra relative to the trace amounts of derivatizing linker molecules present (the Au or Ag-NPs will be IR inactive) but also, by the metal-surface selection rule, only groups where

288 the oscillating dipole moment is perpendicular to the surface will be observed (Greenler et al., 1982).
289 Hence, not all adsorbed bands will be observed depending on the linker-to-surface orientation which
290 typically defaults to parallel to the surface (Le Ru *et al*., 2011). Bearing these factors in mind, the weak
291 bands at ~1440 cm^{-1} and 2954 cm^{-1} were assigned as the scissoring mode of alkyl-chain CH_2 groups
292 (Yah *et al.*, 2012) and C–H alkyl stretching bands, respectively. Their presence was observed for both
293 morphologies of HNTs@Au-NPs composites using phosphonic-acid linker molecules (Fig. S10). This
294 was consistent with the sorption of the linker molecules (and hence the Au-NPs) on the surface of the
295 HNTs.

296 The present study was able to establish that for the polygonal prismatic sample, normalization to the
297 Si–O band height reduced the intensity of the 3670 cm^{-1} intermediate Al–OH stretching band by up to
298 50%, suggesting that chemisorption to produce phosphonate esters (Fig. 2, Fig. S10) took place at these
299 sites. These OH-stretching bands (Fig. 2) are further explained in the polygonal morphology by out-of-
300 phase stretching which is split due to an imperfect three-fold symmetry, a phenomenon which is also
301 observed in some kaolinites (Farmer, 1974; Hillier *et al.*, 2016). For the cylindrical morphology (Fig.
302 S10), this effect was less apparent as only two O–H stretching bands are observed in this region at
303 3620 cm^{-1} and 3690 cm^{-1}, as the cylindrical morphology is less crystalline *(Hillier et al.*, 2016).
304 Furthermore, it was not possible to determine the linker-binding mechanism (i.e. mono- or bi-dentate)
305 to the HNTs by FTIR. This is explained when the weak intensity of the much more prevalent C–H-
306 related bands is considered (Fig. S10). For example, there are 24 C–H bonds to one phosphonate group
307 in this linker molecule (12-mercaptododecylphosphonic acid) and the C–H modes are very weak.
308 Hence, the anticipated phosphonate binding groups are below the limit of detection by FTIR. The bands
309 observed at ~3550 cm^{-1} can be assigned to 'hole' water as discussed by Hillier *et al.* (2016).

310 The concentric rings observed in the cylindrical HNT sample by SAED can be explained by the reduced
311 crystallographic ordering between adjacent planes of atoms due to their curved layers. By comparison,
312 the polygonal prismatic sample is likely to show more crystallographic ordering due to the planar nature
313 of its external layers leading to greater long-range order, in turn resulting in the spots observed in the
314 electron diffraction patterns. Similar effects can be seen in XRD when comparing cylindrical and

polygonal prismatic nanotubes (Hillier *et al.*, 2016) showing that multiple analytical methods can be employed to distinguish between the two HNT morphologies.

Comparing the TEM data for Au-NPs sorption onto the cylindrical or polygonal prismatic HNTs, the data showed that for both morphologies the HNTs@Au-NPs composites displayed Au-NPs on the surface of the internal lumina, at the tube termini and on the external surfaces of the tubes. This would appear to be in agreement with previous studies that have shown that the sorption of phosphonic acids occurs on the inner lumina of halloysites, the primary location exposing the aluminol groups (Taroni *et al.,* 2019). We can conclude, therefore, that the Au-NPs observed on the external surface may be indicative of steps and edges along the external surfaces of the HNTs. These features were reported recently using atomic force microscopy (AFM) (Gray-Wannell *et al.*, 2023), which demonstrated that the polygonal prismatic samples appeared to have a greater number of steps and edges, and hence edge aluminol sites, on their outer surfaces when compared to cylindrical samples. In this current study, it is also evident that the polygonal prismatic nanotubes had a greater density of Au-NPs visible on the outer nanotube surfaces and the lumina, whereas the cylindrical nanotubes were much sparser in terms of Au-NPs decoration (Fig. 4). The exceptions to this occurred when the halloysites themselves had lots of defects (Fig. 4c,d) where defects are present as fracturing of nanotubes, for example.

Previous work on solution-sorption experiments (Gray-Wannell *et al.,* 2020) revealed that when normalized to the surface area, cylindrical nanotubes had greater phosphate-sorption capacity than their polygonal prismatic counterparts due to their smaller size and hence greater surface area. The lesser extent of Au-NPs sorption observed here is probably due to the larger size of the Au-NPs relative to phosphate anions such that, on the smaller cylindrical HNTs, Au-NPs sorption results in greater steric repulsion between the Au-NPs. In turn, this led to the appearance of more Au-NPs on the larger polygonal prismatic HNTs. Given that the TEM data are qualitative as opposed to quantitative, a clear conclusion can be drawn that, when phosphonate groups are anchored to Au-NPs, the polygonal prismatic HNTs showed greater affinity for sorption than their cylindrical counterparts as depicted in Fig. 4 and, graphically, in Fig. 7.

The TEM analysis showed the difference in behavior between the Au and Ag nanoparticles, where the Ag nanoparticles in the HNTs@Ag-NPs formed agglomerates containing hundreds of NPs. There were several possible explanations for this. The first considered that the PVP/Ag ratio used in the NP-linker synthesis was too high (Wiley *et al.,* 2005). A second hypothesis considered that due to the harder Lewis acid nature of silver in comparison to gold, the Ag-NPs was more attracted to the phosphonic acid/carboxylate anions than the aluminol surface groups on the halloysite nanotubes, which resulted in agglomerates between Ag-NPs and linker molecules of nearby Ag-NPs. The third hypothesis suggested that the loading of the linker molecule may also have an effect where, after a certain loading concentration, the linker molecules began to link Ag-NPs, as opposed to adsorbing onto the halloysite surface, as demonstrated by the oxalate linkage in TiO_2 nanoparticles (Charbonneau *et al.*, 2015). The significance of the different behaviors of the Au- and Ag-NPs in the HNTs@Au-NPs and HNTs@Ag-NPs composites was highlighted when considering the practical applications of this type of work; further work is required to determine whether changing the experimental conditions would result in a different Ag-NPs dispersion on the HNTs surfaces, particularly by determining whether larger Ag-NPs may result in less agglomeration (Jana *et al*., 2017).

(Level 1) Conclusions

The present study has presented a method for the direct observation of surface sorption sites on two different morphologies of HNTs by combining the resolving power of TEM of HNTs@Au-NPs/HNTs@Ag-NPs, which have been surface engineered, with pendant phosphonate or carboxylate linker groups to mimic phosphate or carboxylate sorption, respectively. The data show that the presence of Au-NPs on the external surfaces, inner lumen, and edge sites of the HNTs depend on the polygonal or cylindrical HNT morphology. Interestingly, polygonal prismatic HNTs, which have been shown previously to have more external surface features (Gray-Wannell *et al.,* 2023), displayed greater Au-NPs sorption. By comparison, the smaller cylindrical HNTs displayed less Au-NPs sorption which can be hypothesized as due to steric effects of the Au-NPs. In the present study, for the HNTs@Ag-NPs, the Ag-NPs formed clusters/agglomerations at the surfaces of the polygonal HNTs. The data suggested that the polyvinylpyrrolidone and DMF used in the Ag-NPs synthesis complicated the

interaction of the linker groups with these metal nanoparticles. The sorption of carboxylate or phosphonic acid functionalized Au-NPs, but not for the methyl-terminated linker groups, also supporting the suggestion that chemisorption was being measured via the formation of ester groups with surface hydroxyls rather than physisorption. In summary, the present work highlighted the fundamental importance of understanding the detailed effect of the morphology of the nanotube (Gray-Wannell *et al*., 2023) which impacts on the efficacy of halloysite nanotubes as stable support materials for use in catalytic technologies for Au-NPs, pollutant sorption or drug delivery and/or antibacterial functions when Ag-NPs are considered.

(level 1) **Acknowledgments**

The authors acknowledge external user funding from the Sir Henry Royce Institute and the Leeds EPSRC Nanoscience and Nanotechnology User Facility (EPSRC Grant EP/R02863X/1), which allowed access to TEM facilities at the University of Leeds. NGW acknowledges the support of the Macaulay Development Trust for her PhD funding. NGW and SH acknowledge support from the Rural & and Environment Science & Analytical Services Division of the Scottish Government.

Author Contributions

NGW – conceptualization, methodology, investigation, analysis, writing – original draft. CK – methodology, investigation, writing – review and editing. ZA – TEM investigation, writing – review and editing. JM – XPS investigation, writing- review and editing. SH – supervision, writing – review and editing. CG - supervision, writing – review and editing. RB – funding acquisition, writing – review and editing. PJH – conceptualization, supervision, writing – review and editing.

Conflicts of interest

There are no conflicts of interest to declare.

393 **Figures and Tables**

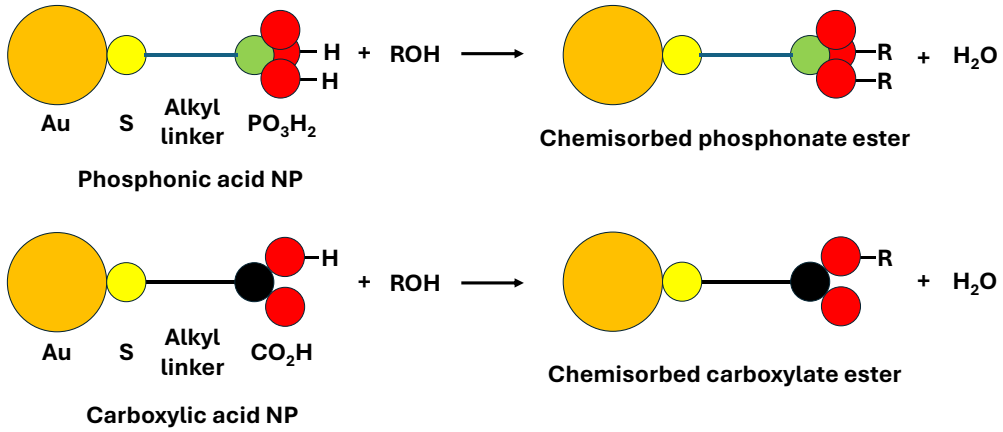

394

395 **Figure 1**. Reaction scheme showing derivatized Au-NPs chemisorbing to halloysite surface hydroxyl

396 groups (R = halloysite).

397

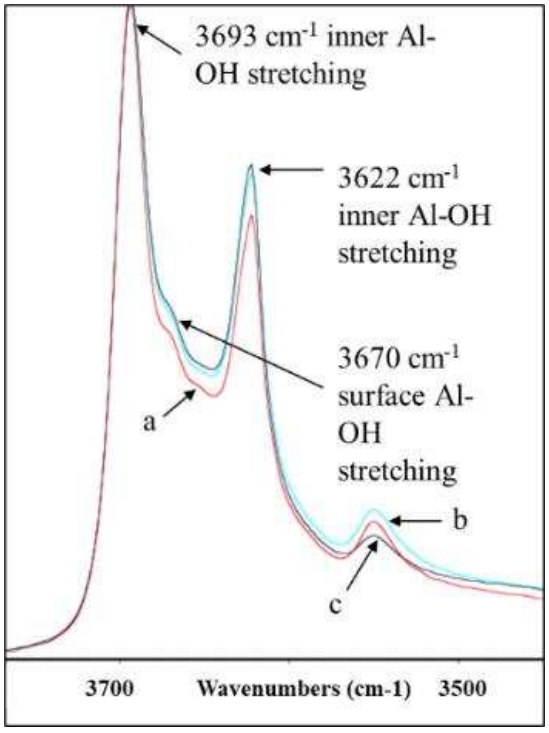

398

399 **Figure 2**. FTIR spectra showing the out-of-phase stretching Al–OH bands present in the polygonal

400 prismatic HNTs in the discreet hydroxyl region from 3400–3800 cm^{-1} of: (a) polygonal prismatic

401 HNTs@Au-NPs with a phosphonic acid terminated linker; (b) polygonal prismatic HNTs after reaction

402 with Au-NPs and a methyl terminated linker; and (c) original polygonal prismatic HNT material.

403

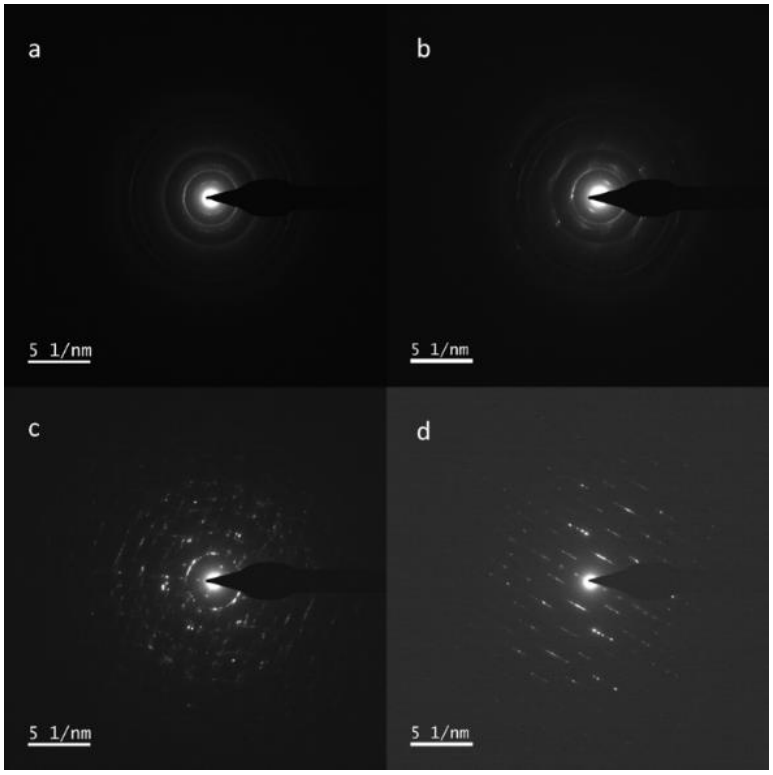

404

405 **Figure 3**. SAED images for: (a) cylindrical HNT; (b) cylindrical HNTs@Au-NPs; (c) prismatic HNT;

406 and (d) prismatic HNTs@Au-NPs.

407

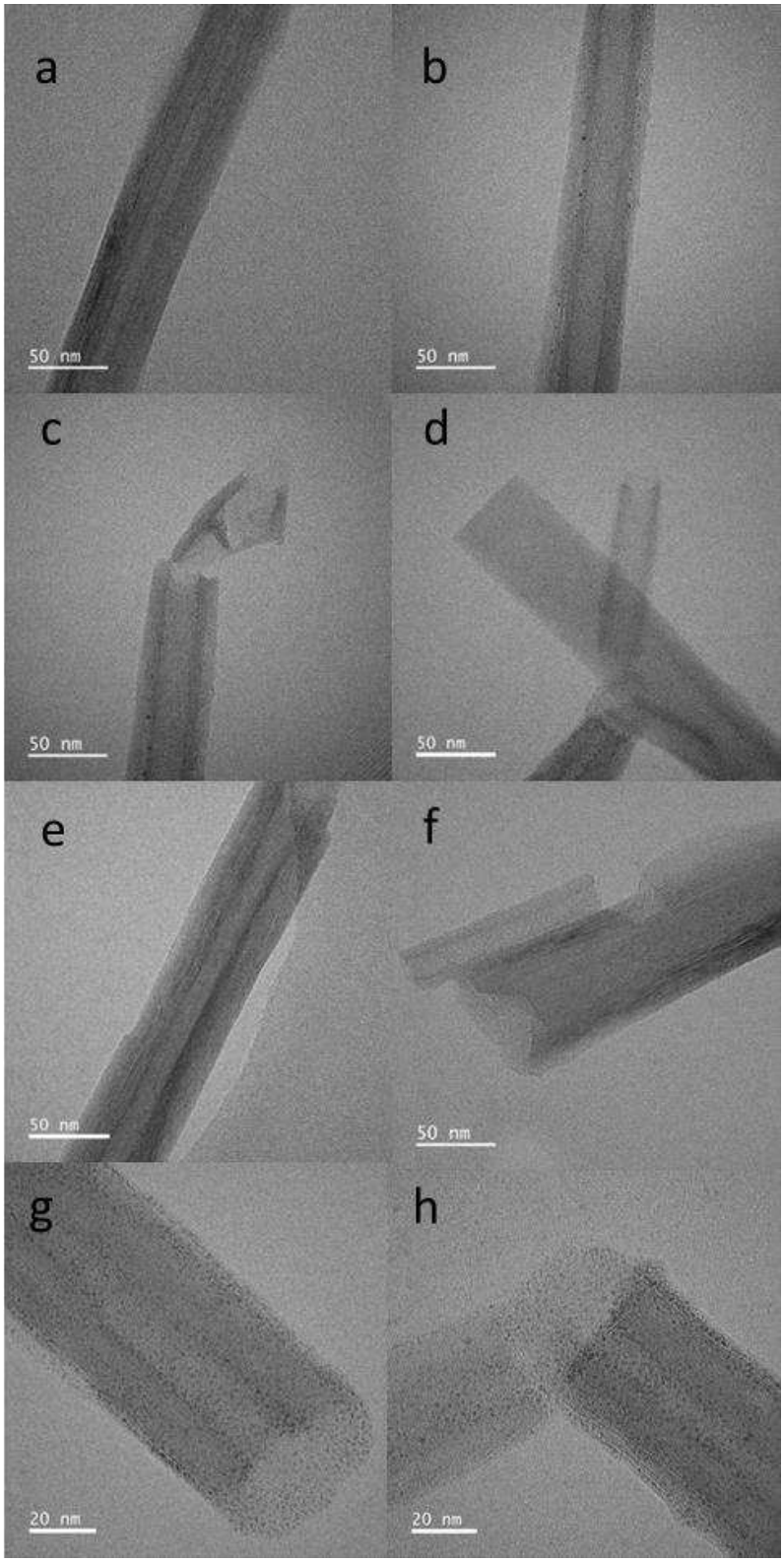

Figure 4. TEM images of the cylindrical and polygonal prismatic halloysite nanotubes in their untreated form and after treatment with Au-NPs and a phosphonic acid terminated inker: (a) cylindrical HNT

411 before treatment; (b–d) cylindrical HNTs@Au-NPs; (e) polygonal HNT before treatment; (f–h)
412 polygonal HNTs@Au-NPs.

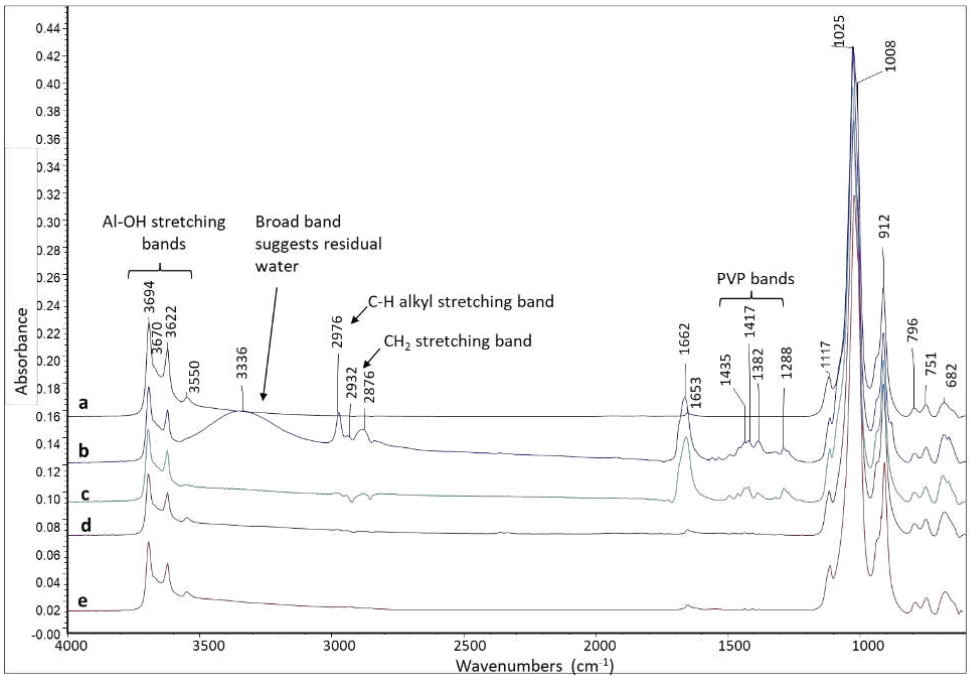

413

414 **Figure 5**. FTIR spectra of polygonal prismatic halloysite with and without Au/Ag-NPs: (a) original
415 material; (b) HNTs@Ag-NPs with a carboxylate terminated linker; (c) HNTs@Ag-NPs with a
416 phosphonic acid terminated linker; (d) HNTs@Au-NPs with a carboxylate terminated linker; and (e)
417 HNTs@Au-NPs with a phosphonic acid terminated linker.

418

419

420

421

422

423

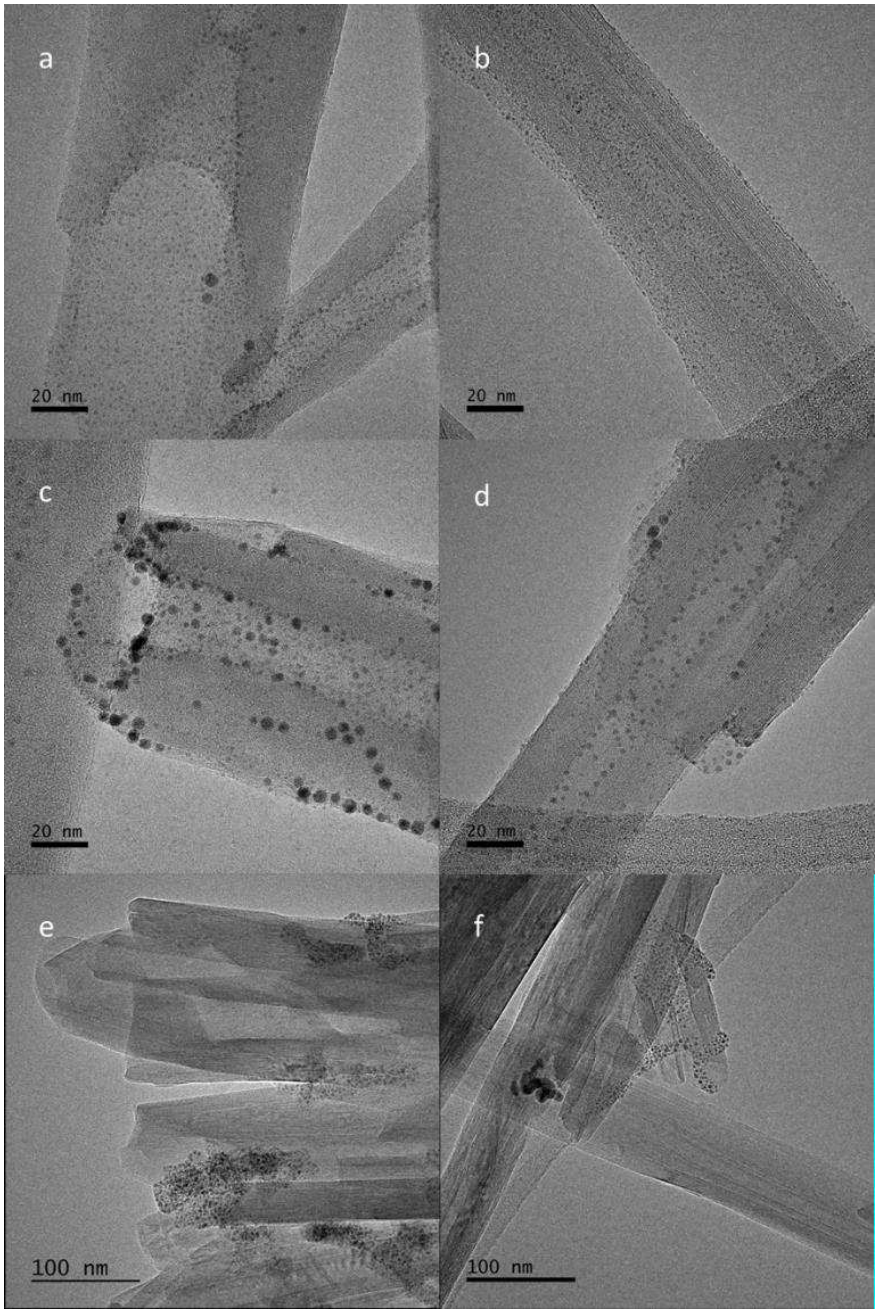

Figure 6. TEM images of polygonal HNT: (a–b) HNTs@Au-NPs and a phosphonic acid-terminated linker; (c–d) HNTs@Au-NPs and a carboxylate-terminated linker; (e) HNTs@Ag-NPs and a phosphonic acid-terminated linker; and (f) HNTs@Ag-NPs and a carboxylate-terminated linker.

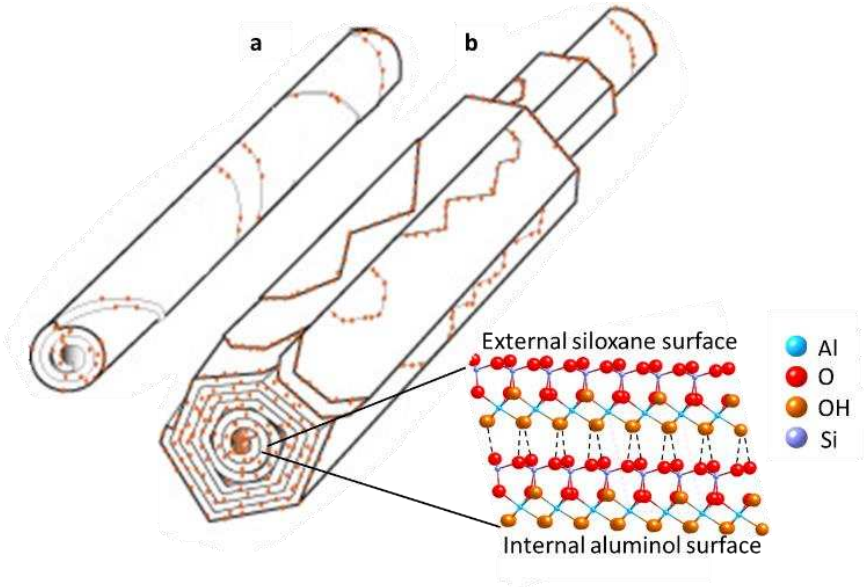

Figure 7. Graphical depiction of the distinction between the: (a) cylindrical and (b) polygonal prismatic HNTs@Au-NPs sorption with phosphonic acid linkers, with the crystalline structure of each HNT layer indicated.

Table 1. XPS data (elements shown as at.% and normalized to the removal of carbon)

	HNT scaffold					**Au nanoparticles**			
Sample	**Al**	**Si**	**Na**	**O_{ox}**	**O_{org}**	**Au**	**P_{met}**	**P_{org}**	**S**
Polygonal prismatic HNT	14.3	16.0	0.6	59.2	10.0	0.0	0.0	0.0	0.0
Cylindrical HNT	15.1	16.1	0.4	61.3	7.1	0.0	0.0	0.0	0.0
Polygonal prismatic HNT									
Au-NP methyl-terminated linker	15.6	17.1	0.0	63.4	3.8	0.1	0.0	0.0	0.0
Au-NP phosphate-terminated linker	13.5	15.5	0.0	59.3	8.8	1.4	0.4	0.8	0.3
Cylindrical HNT									
Au-NP methyl-terminated linker	17.1	18.3	0.1	61.7	2.8	0.0	0.0	0.0	0.0
Au-NP phosphate-terminated linker	16.9	18.2	0.1	55.8	6.6	1.3	0.5	0.4	0.2

Si from SiO_4 groups, O_{ox} = metal oxide, O_{org} = organic, P_{met} = M-phosphonate, P_{org} = PX_3 organic, S from thiol groups

Bibliography

Atyaksheva, L. F., & Kasyanov, I. A. (2021). Halloysite, Natural Aluminosilicate Nanotubes: Structural Features and Adsorption Properties (A Review). *Petroleum Chemistry*, **61**(8), 932-950. https://doi.org/10.1134/S0965544121080119

Bertolino, V., Cavallaro, G., Milioto, S., & Lazzara, G. (2020). Polysaccharides/Halloysite nanotubes for smart bionanocomposite materials. *Carbohydrate Polymers*, **245**, 116502. https://doi.org/https://doi.org/10.1016/j.carbpol.2020.116502

Boraei, S. B. A., Eshghabadi, F., Hosseinpour, R., Zare, Y., Munir, M. T., & Rhee, K. Y. (2024). Halloysite nanotubes in biomedical applications: Recent approaches and future trends. *Applied Clay Science*, **253**, 107346. https://doi.org/https://doi.org/10.1016/j.clay.2024.107346

Burridge, K., Johnston, J., & Borrmann, T. (2011). Silver nanoparticle–clay composites [10.1039/C0JM02702B]. *Journal of Materials Chemistry*, **21**(3), 734-742. https://doi.org/10.1039/C0JM02702B

Calvino, M. M., Lisuzzo, L., Cavallaro, G., Lazzara, G., Yadav, R. P., Dolgan, K., & Lvov, Y. M. (2025). The Emerging Role of Halloysite Clay Nanotube Formulations in Cosmetics and Topical Drug Delivery. *ACS Applied Bio Materials*, **8**(4), 2674-2690. https://doi.org/10.1021/acsabm.4c01938

Cao, H., Sun, X., Zhang, Y., & Jia, N. (2012). Electrochemical sensing based on gold nanoparticle-decorated halloysite nanotube composites. *Analytical Biochemistry*, **430**(2), 111-115. https://doi.org/https://doi.org/10.1016/j.ab.2012.08.014

Charbonneau, C., Holliman, P. J., Davies, M. L., Watson, T. M., & Worsley, D. A. (2015). Facile self-assembly and stabilization of metal oxide nanoparticles. *Journal of Colloid and Interface Science*, **442**, 110-119. https://doi.org/https://doi.org/10.1016/j.jcis.2014.11.042

Danyliuk, N., Tomaszewska, J., & Tatarchuk, T. (2020). Halloysite nanotubes and halloysite-based composites for environmental and biomedical applications. *Journal of Molecular Liquids*, **309**, 113077. https://doi.org/https://doi.org/10.1016/j.molliq.2020.113077

dos Santos, E. C., Rozynek, Z., Hansen, E. L., Hartmann-Petersen, R., Klitgaard, R. N., Løbner-Olesen, A., Michels, L., Mikkelsen, A., Plivelic, T. S., Bordallo, H. N., & Fossum, J. O. (2017). Ciprofloxacin intercalated in fluorohectorite clay: identical pure drug activity and toxicity with higher adsorption and controlled release rate [10.1039/C7RA01384A]. *RSC Advances*, **7**(43), 26537-26545. https://doi.org/10.1039/C7RA01384A

Farmer, V. C. (1974). *The Infrared Spectra of Minerals*. Mineralogical Society of Great Britain and Ireland. https://doi.org/10.1180/mono-4

Goswami, N., Biswas, B., Naidu, R., & Vasilev, K. (2019). Spatially Localized Synthesis of Metal Nanoclusters on Clay Nanotubes and Their Catalytic Performance. *ACS Sustainable Chemistry & Engineering*, **7**(22), 18350-18358. https://doi.org/10.1021/acssuschemeng.9b03887

Gray-Wannell, N., Holliman, P. J., Greenwell, H. C., Delbos, E., & Hillier, S. (2020). Adsorption of phosphate by halloysite (7 Å) nanotubes (HNTs). *Clay Minerals*, **55**(2), 184-193. https://doi.org/10.1180/clm.2020.24

Gray-Wannell, N. B., Cubillas, P., Aslam, Z., Holliman, P. J., Greenwell, H. C., Brydson, R., Delbos, E., Strachan, L.-J., Fuller, M., & Hillier, S. (2023). Morphological features of halloysite nanotubes (HNTs) as revealed by various microscopies. *Clay Minerals*, **58**(4), 395-407. https://doi.org/doi.org/10.1180/clm.2023.37

Greenler, R. G., Snider, D. R., Witt, D., & Sorbello, R. S. (1982). The metal-surface selection rule for infrared spectra of molecules adsorbed on small metal particles. *Surface Science*, **118**(3), 415-428. https://doi.org/https://doi.org/10.1016/0039-6028(82)90197-2

Hillier, S., Brydson, R., Delbos, E., Fraser, T., Gray, N., Pendlowski, H., Phillips, I., Robertson, J., & Wilson, I. (2016). Correlations among the mineralogical and physical properties of halloysite nanotubes (HNTs). *Clay Minerals*, **51**(3), 325-350. https://doi.org/10.1180/claymin.2016.051.3.11

Huang, S.-W., Lin, Y.-F., Li, Y.-X., Hu, C.-C., & Chiu, T.-C. (2019). Synthesis of Fluorescent Carbon Dots as Selective and Sensitive Probes for Cupric Ions and Cell Imaging. *Molecules*, **24**(9), 1785. https://www.mdpi.com/1420-3049/24/9/1785

Jana, S., Kondakova, A. V., Shevchenko, S. N., Sheval, E. V., Gonchar, K. A., Timoshenko, V. Y., & Vasiliev, A. N. (2017). Halloysite nanotubes with immobilized silver nanoparticles for anti-bacterial application. *Colloids and Surfaces B: Biointerfaces*, **151**, 249-254. https://doi.org/https://doi.org/10.1016/j.colsurfb.2016.12.017

Joussein, E., Petit, S., Churchman, J., Theng, B., Righi, D., & Delvaux, B. (2005). Halloysite clay minerals — a review. *Clay Minerals*, **40**(4), 383-426. https://doi.org/10.1180/0009855054040180

Kornilova, A. V., Kuralbayeva, G. A., Stavitskaya, A. V., Gorbachevskii, M. V., Karpukhina, O. V., Lysenko, I. V., Pryadun, V. V., Novikov, A. A., Vasiliev, A. N., & Timoshenko, V. Y. (2021). Gold nanoparticles immobilized on halloysite nanotubes for spatially-temporally localized photohyperthermia. *Applied Surface Science*, **566**, 150671. https://doi.org/https://doi.org/10.1016/j.apsusc.2021.150671

Kumar-Krishnan, S., Hernandez-Rangel, A., Pal, U., Ceballos-Sanchez, O., Flores-Ruiz, F. J., Prokhorov, E., Arias de Fuentes, O., Esparza, R., & Meyyappan, M. (2016). Surface functionalized halloysite nanotubes decorated with silver nanoparticles for enzyme immobilization and biosensing [10.1039/C6TB00051G]. *Journal of Materials Chemistry B*, **4**(15), 2553-2560. https://doi.org/10.1039/C6TB00051G

Le Ru, E. C., Meyer, S. A., Artur, C., Etchegoin, P. G., Grand, J., Lang, P., & Maurel, F. (2011). Experimental demonstration of surface selection rules for SERS on flat metallic surfaces [10.1039/C1CC10484E]. *Chemical Communications*, **47**(13), 3903-3905. https://doi.org/10.1039/C1CC10484E

Li, Y., Liu, S., Yao, T., Sun, Z., Jiang, Z., Huang, Y., Cheng, H., Huang, Y., Jiang, Y., Xie, Z., Pan, G., Yan, W., & Wei, S. (2012). Controllable synthesis of gold nanoparticles with ultrasmall size and high monodispersity via continuous supplement of precursor [10.1039/C2DT31270K]. *Dalton Transactions*, **41**(38), 11725-11730. https://doi.org/10.1039/C2DT31270K

Lin, Y., Wang, X., Liu, J., & Miller, J. D. (2017). Natural halloysite nano-clay electrolyte for advanced all-solid-state lithium-sulfur batteries. *Nano Energy*, **31**, 478-485. https://doi.org/https://doi.org/10.1016/j.nanoen.2016.11.045

Lvov, Y., Wang, W., Zhang, L., & Fakhrullin, R. (2016). Halloysite Clay Nanotubes for Loading and Sustained Release of Functional Compounds. *Advanced Materials*, **28**(6), 1227-1250. https://doi.org/https://doi.org/10.1002/adma.201502341

Mallick, K., Witcomb, M., & Scurrell, M. (2006). Silver nanoparticle catalysed redox reaction: An electron relay effect. *Materials Chemistry and Physics*, **97**(2), 283-287. https://doi.org/https://doi.org/10.1016/j.matchemphys.2005.08.011

Massaro, M., Colletti, C. G., Fiore, B., La Parola, V., Lazzara, G., Guernelli, S., Zaccheroni, N., & Riela, S. (2019). Gold nanoparticles stabilized by modified halloysite nanotubes for catalytic applications. *Applied Organometallic Chemistry*, **33**(3), e4665. https://doi.org/https://doi.org/10.1002/aoc.4665

Massaro, M., Lazzara, G., Milioto, S., Noto, R., & Riela, S. (2017). Covalently modified halloysite clay nanotubes: synthesis, properties, biological and medical applications [10.1039/C7TB00316A]. *Journal of Materials Chemistry B*, **5**(16), 2867-2882. https://doi.org/10.1039/C7TB00316A

Mazloumi, O., Biabanpour, F. Z., & Nojavan, S. (2025). Halloysite-based sorbents: Synthesis, characterization, and applications in sample preparation. *TrAC Trends in Analytical Chemistry*, **189**, 118241. https://doi.org/https://doi.org/10.1016/j.trac.2025.118241

Melnyk, A., Lazzara, G., & Chyhyrynets, O. (2025). Smart tablets based on halloysite nanotubes for controlled delivery and photoprotection of active pharmaceutical ingredients. *Hybrid Advances*, **9**, 100383. https://doi.org/https://doi.org/10.1016/j.hybadv.2025.100383

Pastoriza-Santos, I., & Liz-Marzán, L. M. (1999). Formation and Stabilization of Silver Nanoparticles through Reduction by N,N-Dimethylformamide. *Langmuir*, **15**(4), 948-951. https://doi.org/10.1021/la980984u

Philip, A., Lihavainen, J., Keinänen, M., & Pakkanen, T. T. (2017). Gold nanoparticle-decorated halloysite nanotubes – Selective catalysts for benzyl alcohol oxidation. *Applied Clay Science*, **143**, 80-88. https://doi.org/https://doi.org/10.1016/j.clay.2017.03.015

Qu, S., Du, C., Song, Y., Wang, Y., Gao, Y., Liu, S., Li, Y., & Zhu, D. (2002). Optical nonlinearities and optical limiting properties in gold nanoparticles protected by ligands. *Chemical Physics Letters*, **356**(3), 403-408. https://doi.org/https://doi.org/10.1016/S0009-2614(02)00396-2

Rao, K. S., Ganeev, R. A., Zhang, K., Fu, Y., Boltaev, G. S., Maurya, S. K., & Guo, C. (2019). Comparative analyses of optical limiting effects in metal nanoparticles and perovskite nanocrystals. *Optical Materials*, **92**, 366-372. https://doi.org/https://doi.org/10.1016/j.optmat.2019.04.058

Riahi, G., Guillemot, D., Polisset-Thfoin, M., Khodadadi, A. A., & Fraissard, J. (2002). Preparation, characterization and catalytic activity of gold-based nanoparticles on HY zeolites. *Catalysis Today*, **72**(1), 115-121. https://doi.org/https://doi.org/10.1016/S0920-5861(01)00485-0

Sayfutdinova, A. R., Cherednichenko, K. A., Bezdomnikov, A. A., Rodrigues-Filho, U. P., Vinokurov, V. V., Tuleubayev, B., Rimashevskiy, D., Kopitsyn, D. S., & Novikov, A. A. (2023). Antibacterial composites based on halloysite with silver nanoparticles and polyoxometalates. *JCIS Open*, **12**, 100098. https://doi.org/https://doi.org/10.1016/j.jciso.2023.100098

Sharifzadeh, G., Wahit, M. U., Soheilmoghaddam, M., Whye, W. T., & Pasbakhsh, P. (2016). Kappa-carrageenan/halloysite nanocomposite hydrogels as potential drug delivery systems. *Journal of the Taiwan Institute of Chemical Engineers*, **67**, 426-434. https://doi.org/https://doi.org/10.1016/j.jtice.2016.07.027

Shi, Y., Yang, R., & Yuet, P. K. (2009). Easy decoration of carbon nanotubes with well dispersed gold nanoparticles and the use of the material as an electrocatalyst. *Carbon*, **47**(4), 1146-1151. https://doi.org/https://doi.org/10.1016/j.carbon.2008.12.049

Taroni, T., Meroni, D., Fidecka, K., Maggioni, D., Longhi, M., & Ardizzone, S. (2019). Halloysite nanotubes functionalization with phosphonic acids: Role of surface charge on molecule localization and

559 reversibility. *Applied Surface Science*, **486**, 466-473.
560 https://doi.org/https://doi.org/10.1016/j.apsusc.2019.04.264
561 Van Hyning, D. L., & Zukoski, C. F. (1998). Formation Mechanisms and Aggregation Behavior of Borohydride
562 Reduced Silver Particles. *Langmuir*, **14**(24), 7034-7046. https://doi.org/10.1021/la980325h
563 Vergaro, V., Abdullayev, E., Lvov, Y. M., Zeitoun, A., Cingolani, R., Rinaldi, R., & Leporatti, S. (2010).
564 Cytocompatibility and Uptake of Halloysite Clay Nanotubes. *Biomacromolecules*, **11**(3), 820-826.
565 https://doi.org/10.1021/bm9014446
566 Wang, X., Zhu, C., Hu, Y., Zhang, Z., & Zhang, B. (2023). Development and application of cinnamaldehyde-
567 loaded halloysite nanotubes for the conservation of stone cultural heritage. *Applied Clay Science*, **236**,
568 106886. https://doi.org/https://doi.org/10.1016/j.clay.2023.106886
569 Wiley, B., Sun, Y., Mayers, B., & Xia, Y. (2005). Shape-controlled synthesis of metal nanostructures: the case of
570 silver. *Chemistry*, **11**(2), 454-463. https://doi.org/10.1002/chem.200400927
571 Yah, W. O., Takahara, A., & Lvov, Y. M. (2012). Selective Modification of Halloysite Lumen with
572 Octadecylphosphonic Acid: New Inorganic Tubular Micelle. *Journal of the American Chemical*
573 *Society*, **134**(3), 1853-1859. https://doi.org/10.1021/ja210258y
574 Yuan, P., Tan, D., & Annabi-Bergaya, F. (2015). Properties and applications of halloysite nanotubes: recent
575 research advances and future prospects. *Applied Clay Science*, **112-113**, 75-93.
576 https://doi.org/https://doi.org/10.1016/j.clay.2015.05.001
577 Zhang, X. F., Liu, Z. G., Shen, W., & Gurunathan, S. (2016). Silver Nanoparticles: Synthesis, Characterization,
578 Properties, Applications, and Therapeutic Approaches. *International Journal of Molecular Sciences*,
579 **17**(9), 1534. https://doi.org/10.3390/ijms17091534
580 Zhang, Z., Shao, C., Zou, P., Zhang, P., Zhang, M., Mu, J., Guo, Z., Li, X., Wang, C., & Liu, Y. (2011). In situ
581 assembly of well-dispersed gold nanoparticles on electrospun silica nanotubes for catalytic reduction of
582 4-nitrophenol [10.1039/C0CC05693F]. *Chemical Communications*, **47**(13), 3906-3908.
583 https://doi.org/10.1039/C0CC05693F

584

Probing halloysite nanotube (HNT) sorption sites using surface engineered gold or silver nanoparticles – effects of halloysite morphology and binding groups

Nia Gray-Wannell[1], Christopher P. Kershaw[2], Zabeada Aslam[3], James McGettrick[2], Stephen J. Hillier[1,4], Chris Greenwell[5], Rik Brydson[3], and Peter J. Holliman[2]

[1] The James Hutton Institute, Craigiebuckler, Aberdeen, AB15 8QH, UK

[2] Faculty of Science and Engineering, Swansea University, Bay Campus, Swansea, SA1 8EN, UK

[3] School of Chemical and Process Engineering, University of Leeds, Leeds, LS2 9JT, UK

[4] Department of Soil and Environment, Swedish University of Agricultural Sciences, P.O. Box 7014, SE-75007 Uppsala, Sweden

[5] Department of Earth Sciences, Durham University, Durham, DH1 3LE, UK

Corresponding author: Nia Gray-Wannell; Email: nia.gray-wannell@hutton.ac.uk

SUPPLEMENTARY INFORMATION

Table S1. XPS quantification, data prior to C-normalization. The following peaks were analysed: C 1s, Al 2p, Si 2p, O 1s, P 2p, Na 1s, Au 4f.

Sample	Elements from halloysite scaffold (atom%)						Elements from Au NPs (atom%)			
	Si SiO4	Al	O Mox	O organic	C	Na	Au	P phosphonate	P organic	S thiol
Pristine halloysite										
Polygonal prismatic	10.4	9.3	38.6	6.5	34.8	0.4	ND	ND	ND	ND
Cylindrical HNT	15.2	14.3	57.9	6.7	5.6	0.4	ND	ND	ND	ND
Polygonal prismatic HNT after sorption										
Au-NP-methyl terminated linker	16.0	14.6	59.3	3.6	6.4	ND	0.07	ND	ND	ND
Au-NP-phosphate terminated linker	11.8	10.3	45.2	6.7	23.7	0.0	1.06	0.32	0.61	0.21
Cylindrical HNT after sorption										
Au-NP – methyl terminated linker	17.1	16.0	57.6	2.6	6.5	0.1	0.02	ND	ND	ND
Au-NP – phosphate terminated linker	15.0	13.9	45.9	5.4	17.7	0.1	1.03	0.43	0.33	0.18

The results (atomic %) were calculated using the program *CASAXPS*©. ND = not detected

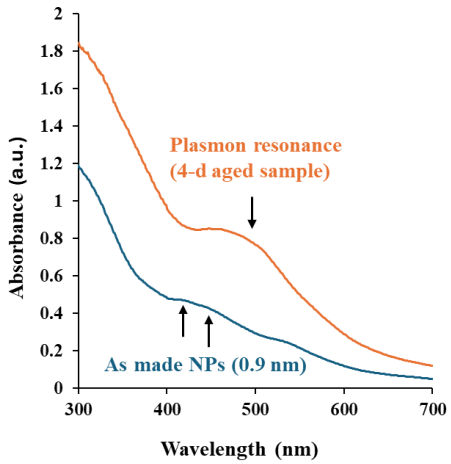

Figure S1. UV-Vis spectra of Au-NPs.

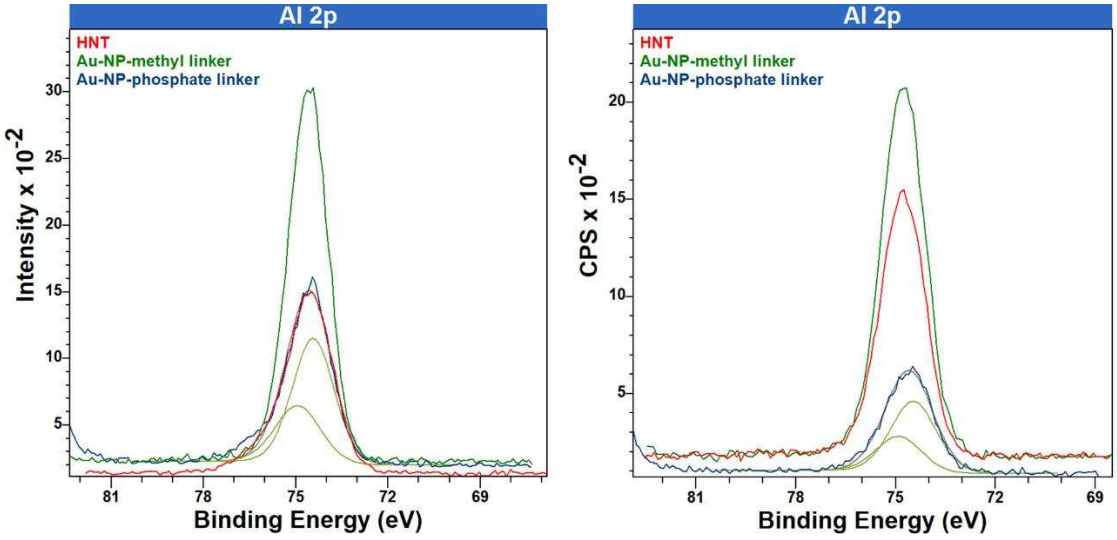

Figure S2. (a) Cylindrical HNTs – Al 2p XPS spectra; (b) polygonal prismatic HNTs – Al 2p XPS spectra.

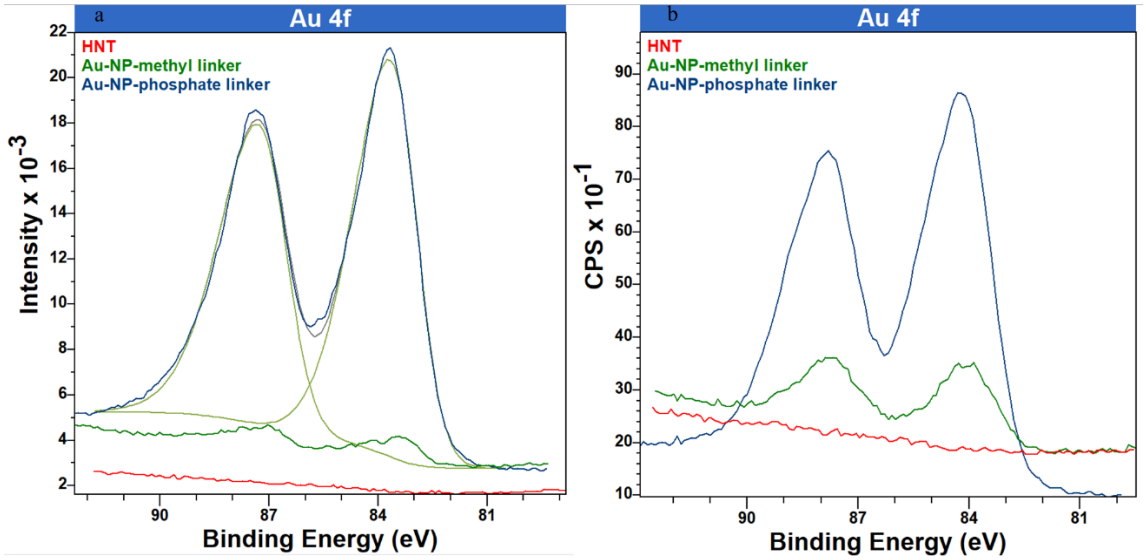

Figure S3. (a) Cylindrical HNTs – Au 4f XPS spectra; (b) polygonal prismatic HNTs – Au 4f XPS spectra.

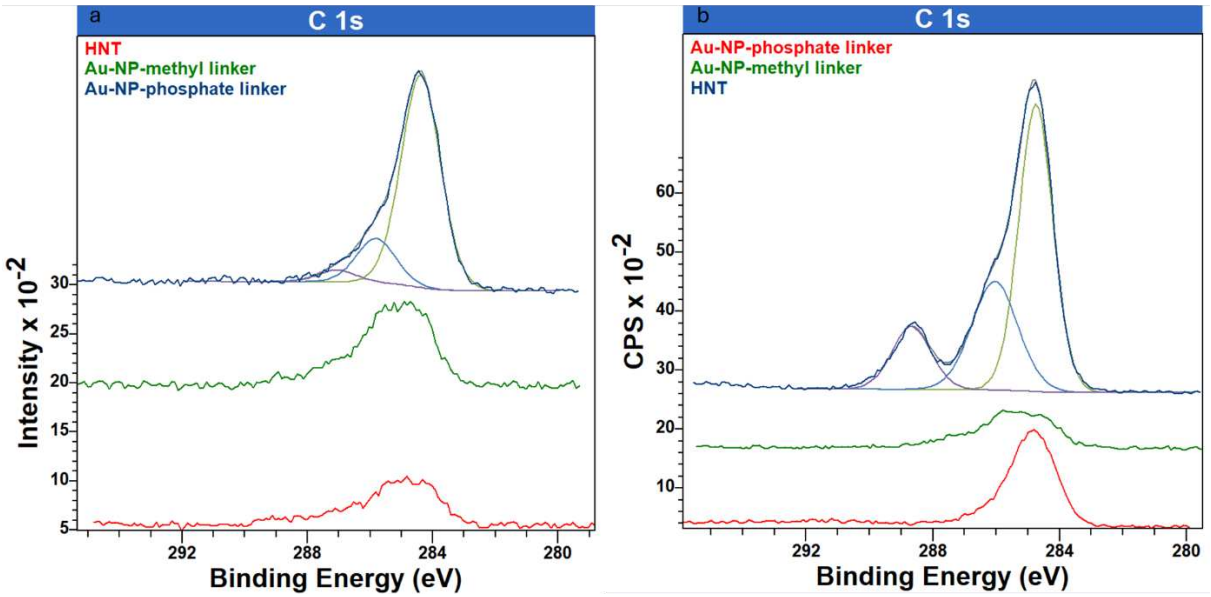

Figure S4. (a) Cylindrical HNTs – C 1s XPS spectra; (b) polygonal prismatic HNTs – C 1s XPS spectra.

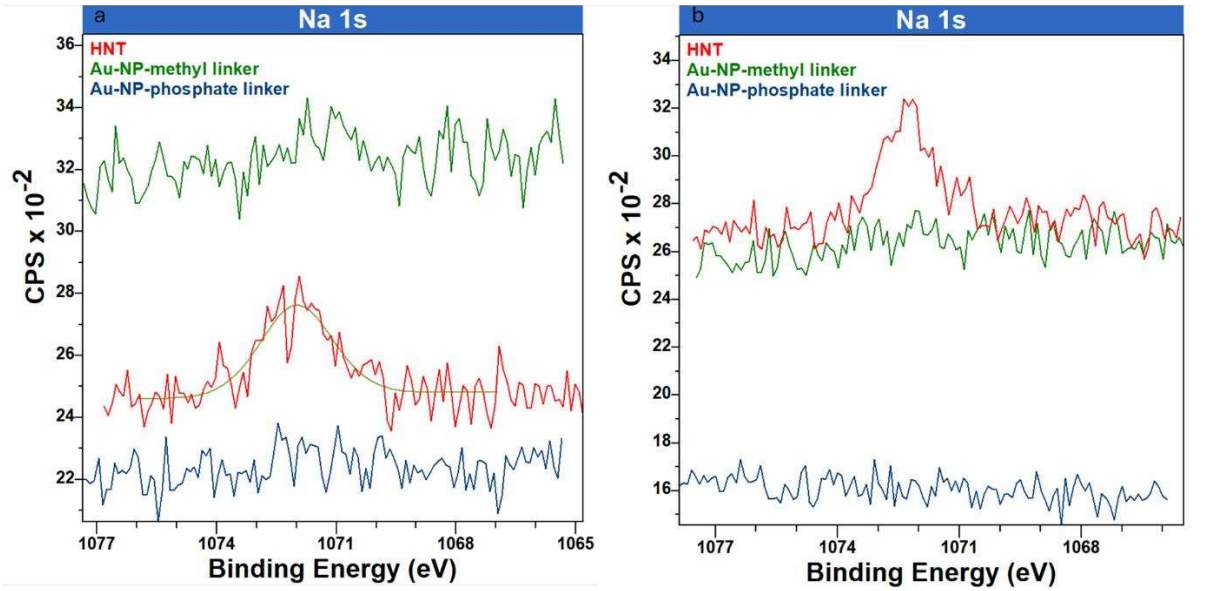

Figure S5. (a) Cylindrical HNTs – Na 1s XPS spectra; (b) polygonal prismatic HNTs – Na 1s XPS spectra.

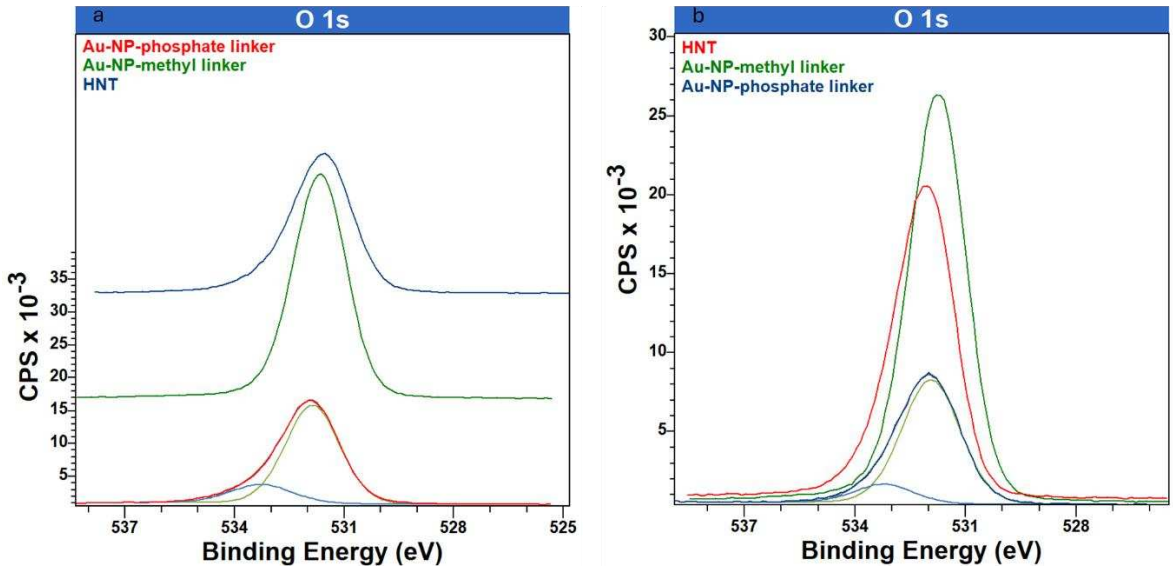

Figure S6. (a) Cylindrical HNTs – O 1s XPS spectra; (b) polygonal prismatic HNTs–O 1s XPS spectra.

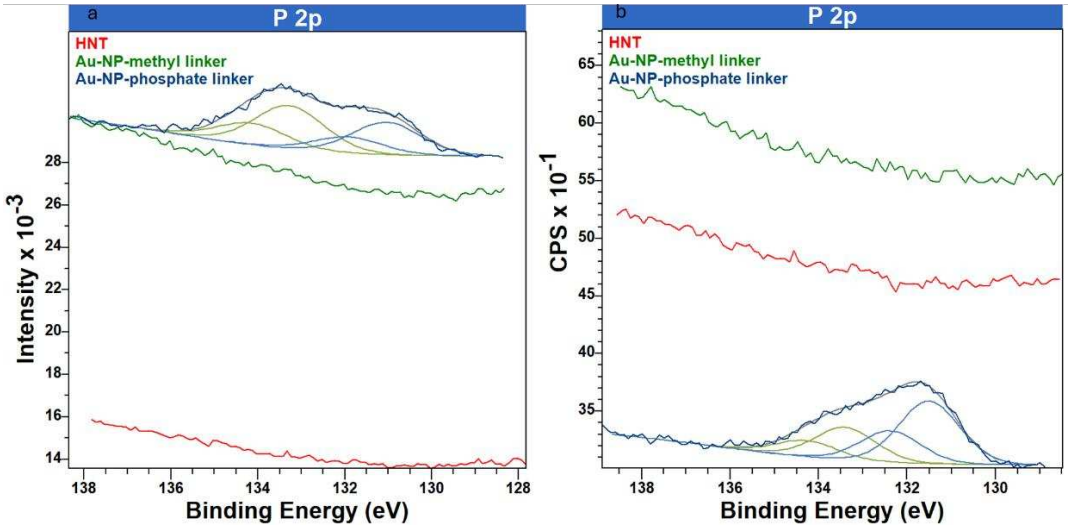

Figure S7. (a) Cylindrical HNTs – P 2p XPS spectra; (b) polygonal prismatic HNTs – P 2p XPS spectra.

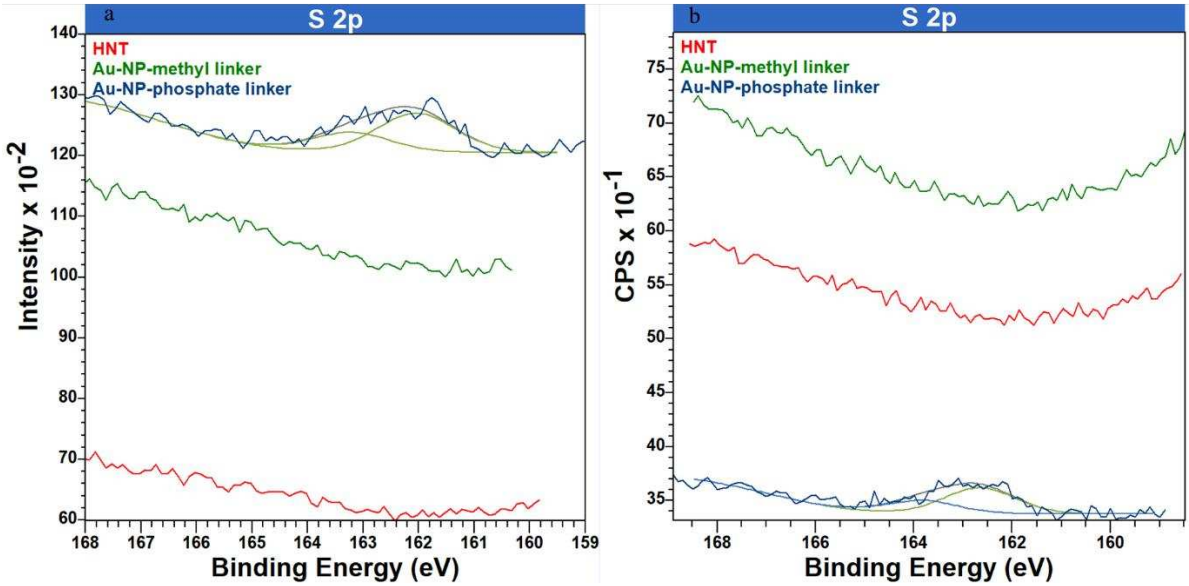

Figure S8. (a) Cylindrical HNTs – S 2p XPS spectra; (b) polygonal prismatic HNTs – S 2p XPS spectra.

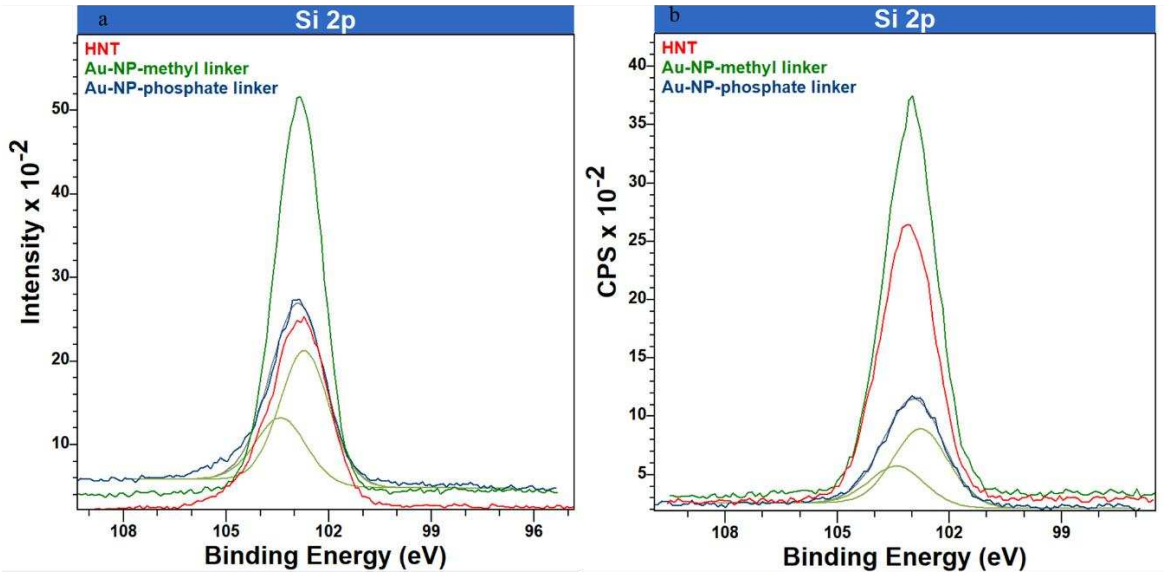

Figure S9. (a) Cylindrical HNTs – Si 2p XPS spectra; (b) polygonal prismatic HNTs – Si 2p XPS spectra.

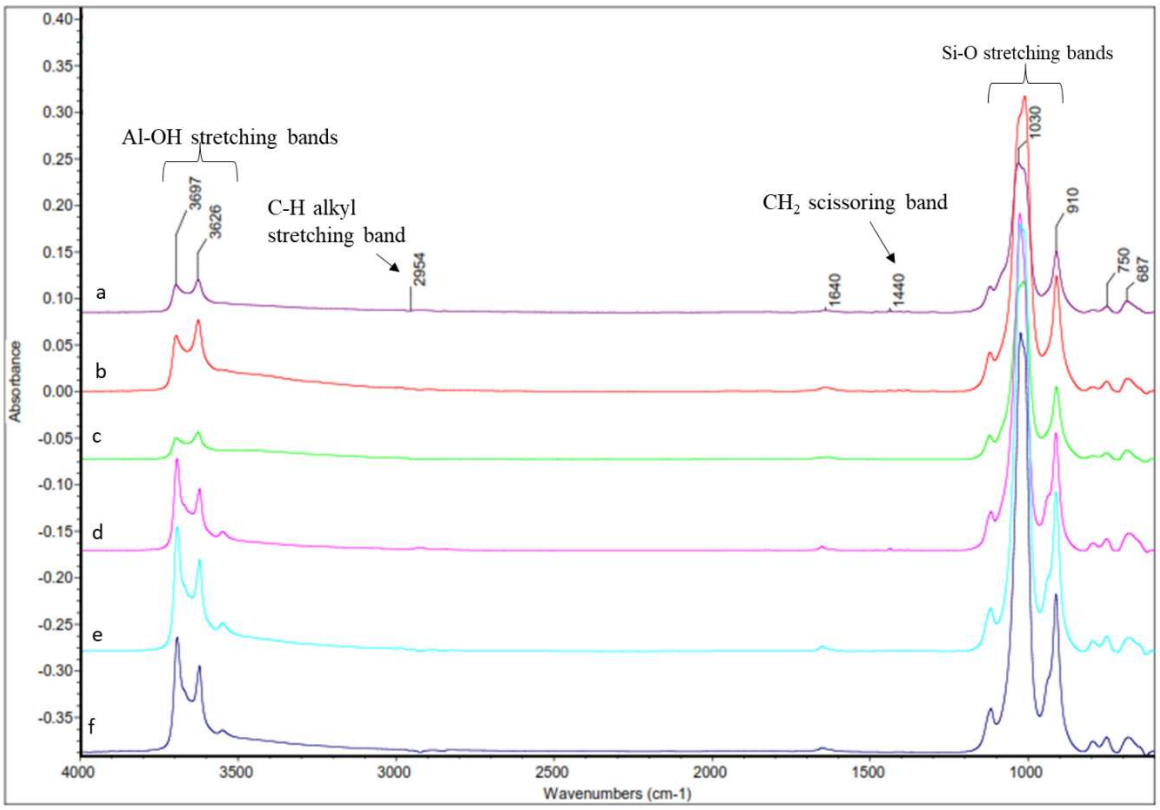

Figure S10. (a) Cylindrical HNTs@Au-NPs with phosphonic acid-terminated linker; (b) cylindrical HNTs@Au-NPs with methyl-terminated linker; (c) cylindrical HNT original material; (d) polygonal prismatic HNTs@Au-NPs with phosphonic acid-terminated linker; (e) polygonal prismatic HNTs@Au-NPs with methyl-terminated linker; (f) polygonal prismatic HNT original material.

Table S2. Selected area electron diffraction data (SAEDP) from TEM and powder X-ray diffraction (XRD) for selected halloysite samples

Sample ID	Halloysite d spacings (Å)												Gold d spacings (Å)		
	(001)		(02,11)		(002)		(02,13)		Not indexed		(06,33)				
	SAEDP	XRD	SAEDP	XRD	SAEDP	XRD	SAEDP	XRD	SAEDP	XRD	SAEDP	XRD	SAEDP		
Pristine halloysites															
Polygonal prismatic	7.2	7.2	4.3	4.4	3.7	3.6	2.3	2.3-2.6	-	-	1.5	1.5	-	-	-
Cylindrical HNT	7.2	7.2	4.6	4.4	3.6	3.6	2.3	2.3-2.6	1.8	1.7	1.6	1.5	-	-	-
Polygonal prismatic HNT after sorption															
Au-NP-phosphate terminated linker	7.2	-	4.5	-	-	-	2.5	2.3-2.6	-	-	1.5	1.5	-	1.2	0.9
Cylindrical HNT after sorption															
Au-NP-phosphate terminated linker	7.6	-	4.5	-	3.6	-	2.6	2.3-2.6	-	-	1.5		2.4	1.2	-

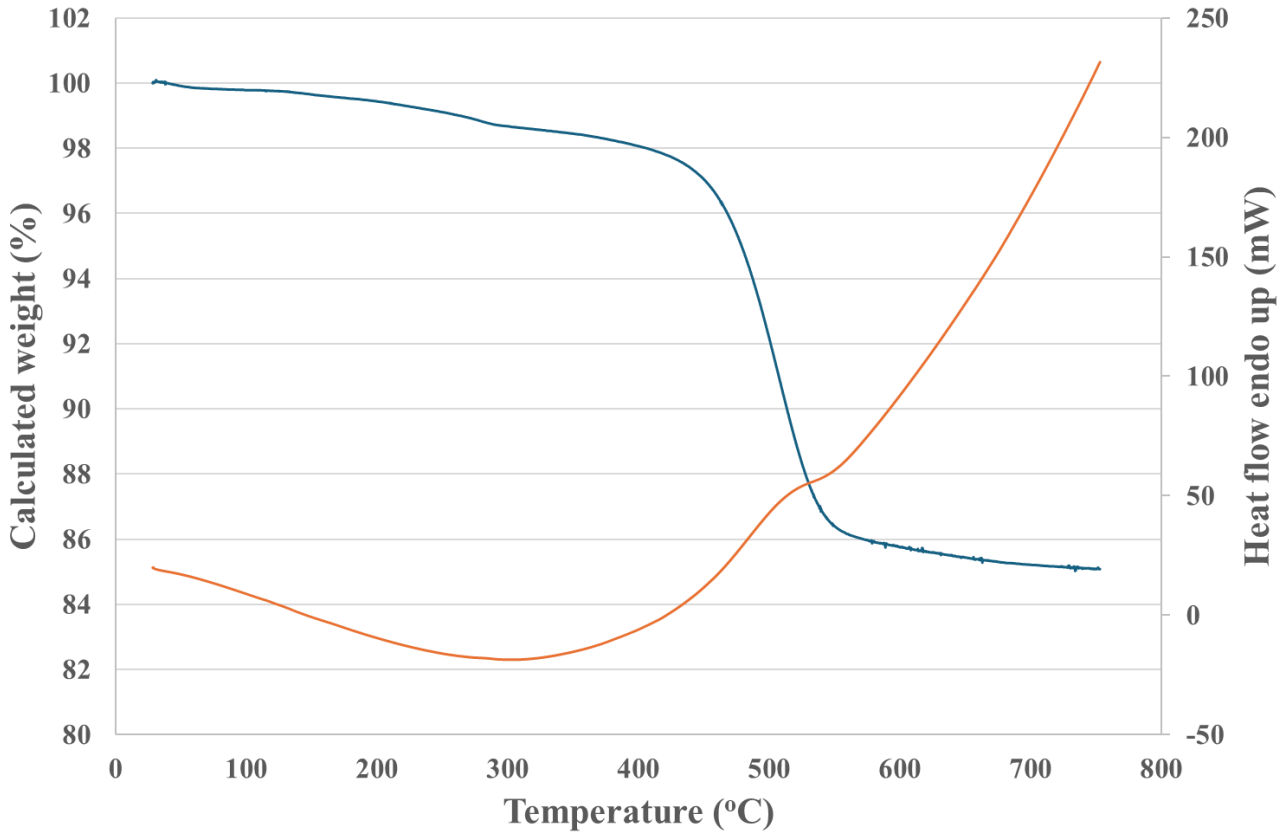

Figure S11. STA analysis of polygonal prismatic HNTs@Au-NPs with methyl-terminated linker.

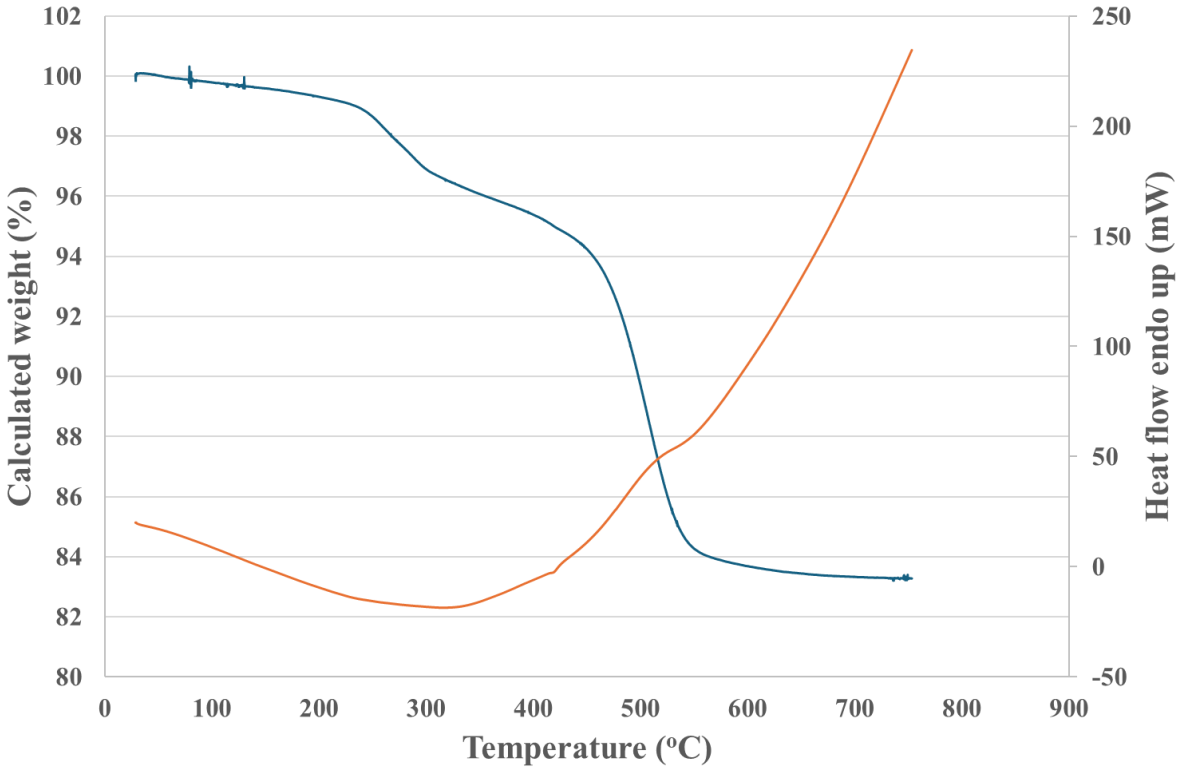

Figure S12. STA analysis of polygonal prismatic HNTs@Au-NPs with phosphonic acid-terminated linker.

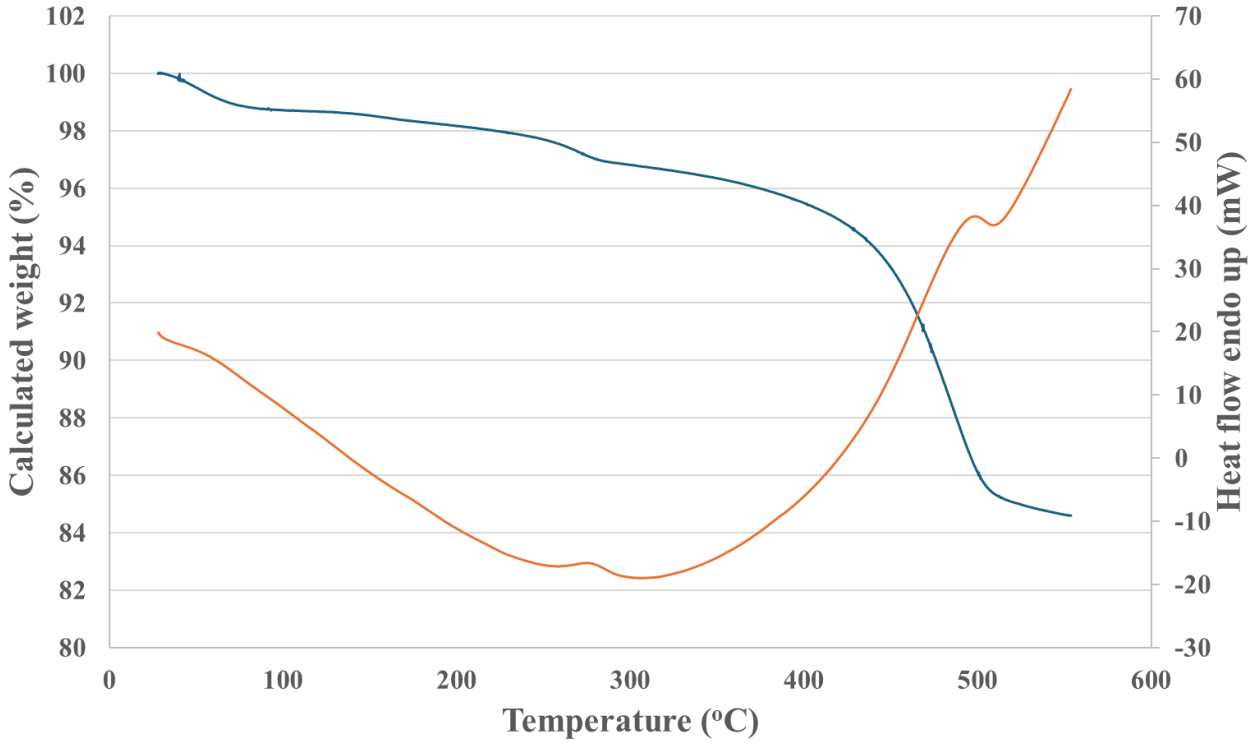

Figure S13. STA analysis of cylindrical HNTs@Au-NPs with methyl-terminated linker.

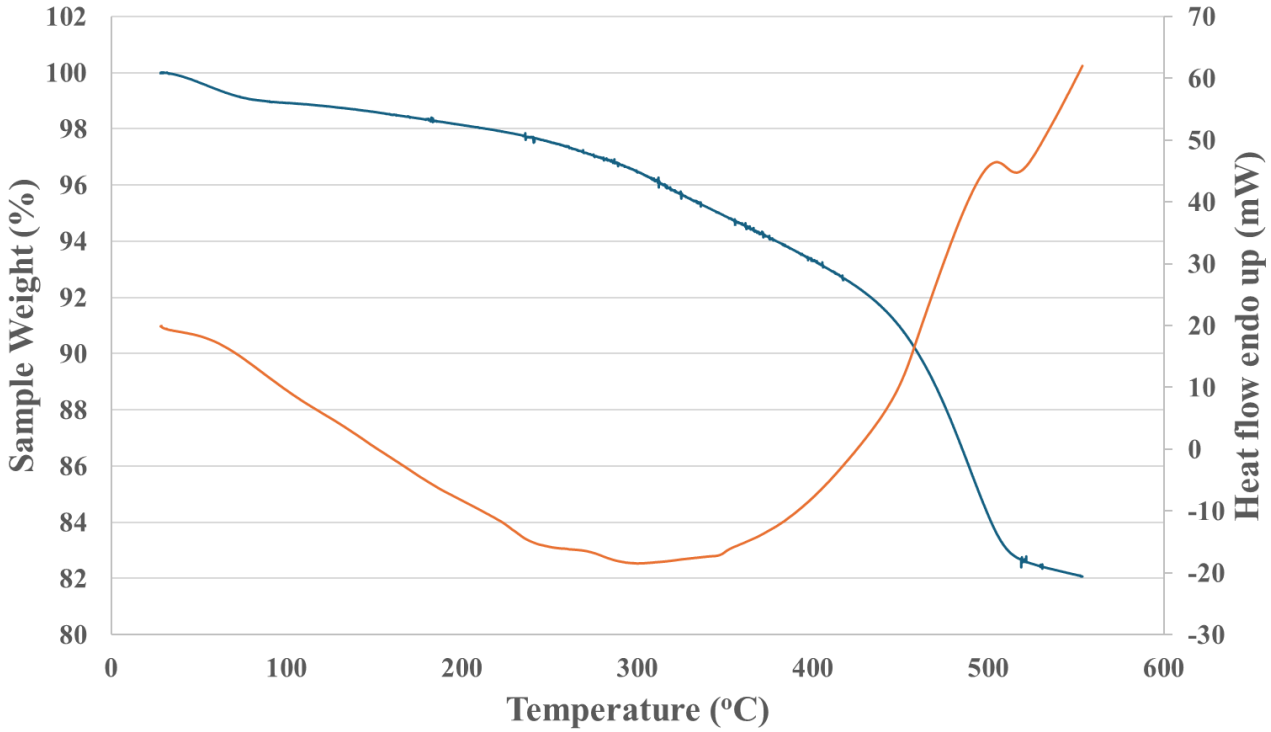

Figure S14. STA analysis of cylindrical HNTs@Au-NPs with phosphonic acid-terminated linker.

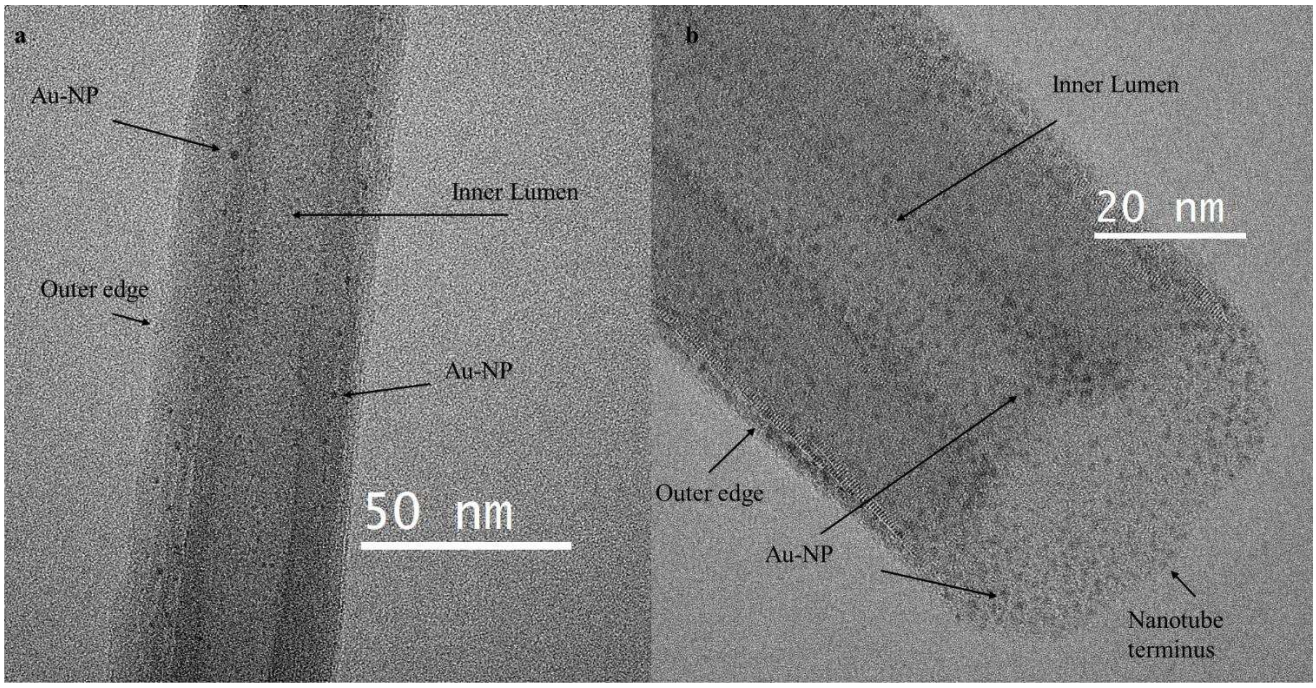

Figure S15. Magnified TEM images of: (a) cylindrical HNTs@Au-NPs; and (b) polygonal prismatic HNTs@Au-NPs.

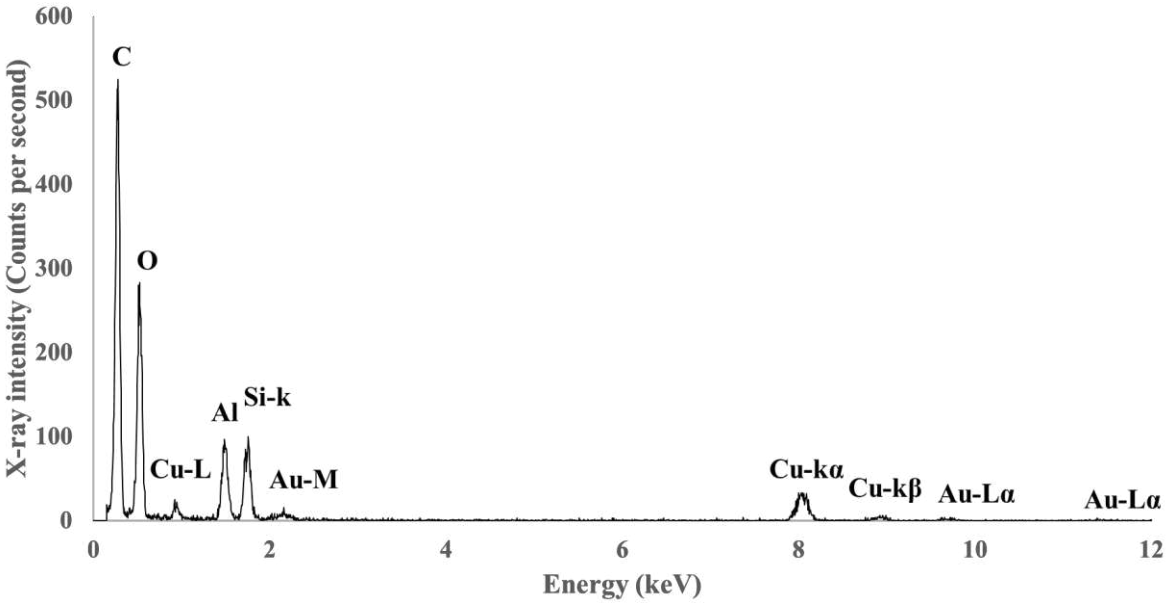

Figure S16. Graph obtained using EDX spectroscopy of polygonal prismatic HNTs@Au-NPs with phosphonic acid-terminated linker.

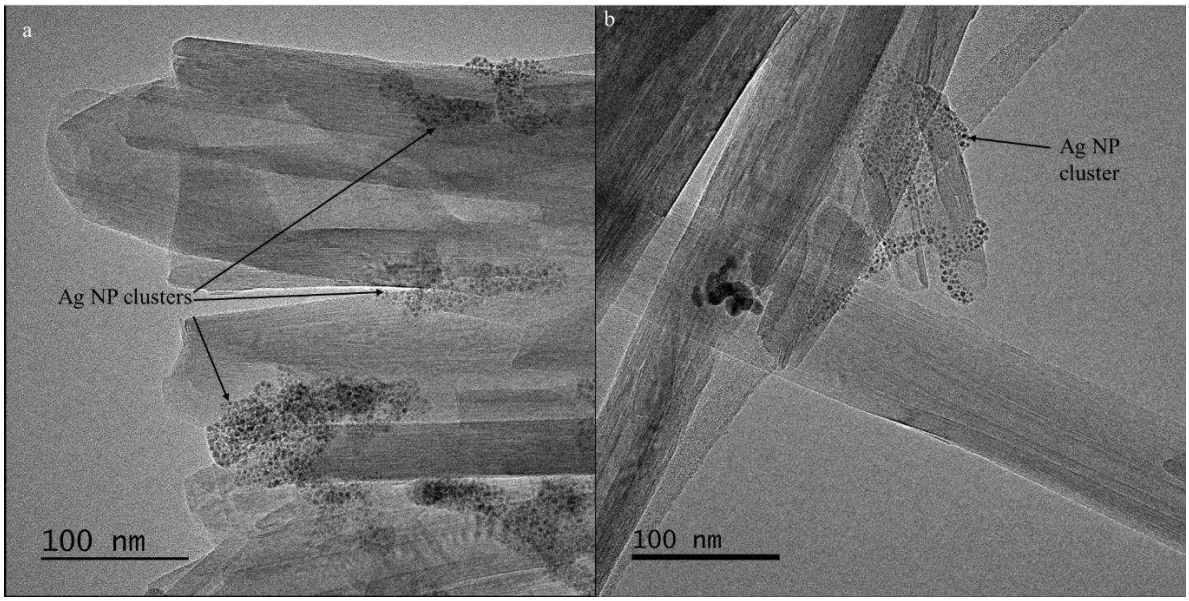

Figure S17. Labeled TEM images of: (a) HNTs@Ag-NPs and phosphonic acid-terminated linker; (b) HNTs@Ag-NPs and carboxylate-terminated linker.